DOE Project

Fate of Methane Emitted from Dissociating Marine Hydrates: Modeling, Laboratory, and Field Constraints

DOE Award Number DE-FE0013999

Final Scientific/Technical Report

Original Period of Performance: 10/01/2013 – 09/30/2016
No-cost Extension: 10/01/2016 – 09/30/2017

Principal Investigator: Ruben Juanes
Massachusetts Institute of Technology

December 31, 2017

Abstract

The overall goals of this research are: (1) to determine the physical fate of single and multiple methane bubbles emitted to the water column by dissociating gas hydrates at seep sites deep within the hydrate stability zone or at the updip limit of gas hydrate stability, and (2) to quantitatively link theoretical and laboratory findings on methane transport to the analysis of real-world field-scale methane plume data placed within the context of the degrading methane hydrate province on the US Atlantic margin.

The project is arranged to advance on three interrelated fronts (numerical modeling, laboratory experiments, and analysis of field-based plume data) simultaneously. The fundamental objectives of each component are the following:

1. Numerical modeling: Constraining the conditions under which rising bubbles become armored with hydrate, the impact of hydrate armoring on the eventual fate of a bubble's methane, and the role of multiple bubble interactions in survival of methane plumes to very shallow depths in the water column.

2. Laboratory experiments: Exploring the parameter space (e.g., bubble size, gas saturation in the liquid phase, "proximity" to the stability boundary) for formation of a hydrate shell around a free bubble in water, the rise rate of such bubbles, and the bubble's acoustic characteristics using field-scale frequencies.

3. Field component: Extending the results of numerical modeling and laboratory experiments to the field-scale using brand new, existing, public-domain, state-of-the-art real world data on US Atlantic margin methane seeps, without acquiring new field data in the course of this particular project. This component quantitatively analyzes data on Atlantic margin methane plumes and place those new plumes and their corresponding seeps within the context of gas hydrate degradation processes on this margin.

TABLE OF CONTENTS

Executive Summary

Methane plumes comprised of individual bubbles are the primary mechanism for transporting large quantities of methane emitted at deep ocean seafloor seeps from underlying dissociating gas hydrates to the ocean-atmosphere system. The ocean water that separates the massive amounts of methane sequestered in the sediment gas hydrate stability zone from the overlying atmosphere has been termed a biofilter owing to microbially-mediated methane oxidation sink that is active in the water column. However, the physical processes that control the final depths that methane plumes reach in the water column are as important as the biogeochemical processes that mediate the amount of methane reaching the atmosphere. Field observations show that some deep-ocean methane plumes reach shallow ocean depths and that dissolved methane is elevated in shallow waters over many seep sites. Such methane is more likely to find a direct path to the atmosphere. To date, studies of the fate of free methane bubbles within the water column (particularly within the water column hydrate stability zone) have been limited to first-order numerical studies and laboratory experiments published in 1981. In terms of field data, seagoing scientists now routinely image methane plumes, but are challenged in using the imagery to quantify methane fluxes or to assess the interaction of plumes with the ocean-atmosphere system.

The work proposed here, which is equally applicable to methane seepage from dissociating gas hydrates/other seeps and inadvertent methane release due to deepwater exploration and production activities, addresses these knowledge gaps through integrated state-of-the-art numerical modeling, modern laboratory experiments, and the analysis of large amounts of public-domain, multifrequency hydroacoustics data on bubble plumes over the degrading US Atlantic margin gas hydrates province. Phase-field numerical modeling examines the role of hydrate armoring in simultaneously slowing bubble rise and reducing the amount of methane diffusion during bubble ascent through a realistic oceanic pressure-temperature field. Laboratory experiments with a (non-flammable) xenon hydrate proxy constrains the rise rate of gaseous and hydrate-armored bubbles as a function of size, determine the conditions that promote armoring, and yield high-frequency acoustic calibrations on these bubbles. Real-world context is provided by extending the modeling and laboratory results to the US Atlantic margin, which contains an estimated 21,000 Tcf gas in place. Since November 2012, hundreds of water column methane plumes and corresponding seafloor seeps have been discovered on the northern US Atlantic margin, with the seeps bimodally clustered at the top of the gas hydrate stability zone (450 to 550 m) and well within the stability zone (1000-1500 m). Quantitative hydroacoustics analysis of public-domain multibeam and split-beam data over these methane plumes constrain the extent of bubble survival in the water column, the bubble size, and other factors. To place the results in the context of the degradation of the Atlantic margin gas hydrate province as a whole, a margin-wide bottom water temperature database is combined with paleo-temperature constraints and existing seismic and lithologic data to elucidate the short- and long-term driving processes for seep formation (e.g., temperature forcing, canyon formation), the amount of hydrate that has or will dissociate, and the integrated regional methane flux as one component of global methane emissions from deepwater gas hydrates.

The report is organized following the three main thrusts of the original proposal, in which we address the following scientific questions:

1. Determine how long individual and multiple methane bubbles survive in the water column (either as methane-filled gas bubbles or hydrate-armored bubbles) using a sophisticated mi-

croscale phase-field model that incorporates the thermodynamic basis of the multiphase (gas-liquid-hydrate) system and is able to capture the coupling between bubble pressure and hydrate formation/dissociation.

2. Explore the parameter space associated with the formation and survival of hydrate-encrusted gas bubbles, the rise rates of gas and hydrate-armored bubbles, and the rate of gas loss from bubbles in a special laboratory apparatus, with monitoring by optical, acoustic, and other sensors. Xenon (Xe), which is a non-reactive, non-flammable Structure I hydrate former that makes gas hydrate at manageable pressure-temperature conditions, is used for these experiments. Acoustic sensors are similar to those used on marine vessels, making the results easily transferrable to field characterization of methane plumes.
3. Use existing, public-domain, multibeam and split-beam echosounder data to analyze methane plume characteristics (e.g., height of bubble rise, characteristic bubble size, depth dependence of bubble target strength) over hundreds of newly-discovered US Atlantic margin seeps and place the methane plumes in the regional context of gas hydrate dynamics on this margin. The analyses constrain the depths at which methane is released into the water column from plume dissolution, the differences between the persistence of plumes originating just inside and just outside the hydrate stability field, and the past and future susceptibility of the gas hydrate province to intermediate ocean warming.

1 Theoretical and computational models of coupled bubble rise and hydrate formation

1.1 Introduction

Methane hydrate is an ice-like solid that forms out of an aqueous solution of water and dissolved methane under moderate pressure and low temperature conditions [Sloan, 2003] [Fig. 1(a)]. A large body of work over the past few decades has established a fundamental understanding of methane hydrate thermodynamics [Sloan and Koh, 2008]. Combining experimental data with free-energy-minimization techniques, current simulators are able to accurately predict the *equilibrium* phase diagram of the water–methane system [e.g., Fig. 1(b)] under a wide range of pressure, temperature and compositional conditions [Ballard, A. L. and Sloan, 2004; Ballard and Sloan, 2004; Huo et al., 2003; Sloan et al., 2010]. *Nonequilibrium* thermodynamic conditions, however, may persist for long times in natural hydrate systems, and need to be better understood. For instance, the equilibrium phase diagram predicts that, under hydrate-forming temperature, two-phase coexistence of hydrate with either methane gas or aqueous solution is energetically favored; three-phase coexistence with gas, liquid and hydrate is only permitted at the triple-point temperature and pressure. In reality, such three-phase coexistence has been observed at many different spatial and temporal scales where the triple point conditions are not satisfied. At the field scale, *in situ* surveys reveal that gas pockets can coexist with hydrate and water within marine sediments for a long period of time [Suess et al., 1999; Liu and Flemings, 2006; Bangs et al., 2011]. At the millimeter scale, both field studies [Topham, 1984; Rehder et al., 2002; Sauter et al., 2006; Rehder et al., 2009; Graves et al., 2015; Wang et al., 2016] and controlled laboratory experiments [Maini and Bishnoi, 1981; Chen et al., 2014, 2016; Warzinski et al., 2014] have shown that a layer of hydrate shell can survive on a gas bubble in water column for extended periods of time. At the micrometer scale, pockets of oversaturated metastable water can coexist with hydrate when formed in the presence of gas bubbles [Chaouachi et al., 2015].

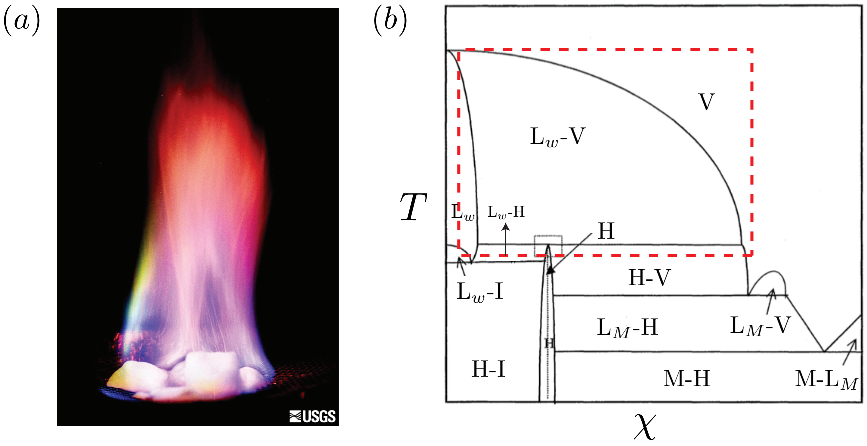

Figure 1. (a) Burning of solid (white) methane hydrate (source: USGS) (b) Isobaric methane–water T–χ phase diagram adapted from [Huo et al., 2003; Sloan et al., 2010].

These nonequilibrium states have long been attributed to a diffusion-limited kinetic effect [Clennell et al., 1999]. However, at the heart of these phenomena is the challenge to understand a rather simple problem: how does hydrate grow on the interface between a hydrocarbon/gas phase and the ambient water phase? Experimental studies have focused on the direction and rate of growth on a macroscopic scale [Taylor et al., 2007; Chen et al., 2014], the influence of sub-cooling and aqueous composition on growth rate Freer et al. [2001]; Tanaka et al. [2009]; Saito et al. [2010] and the micron-scale details of the growth process [Tohidi et al., 2001; Chaouachi et al., 2015; Hauge et al., 2016]. Numerical studies have focused on developing parameterized kinetic growth models [Abay and Svartaas, 2011; Abe et al., 2016]. What is missing is an integrated modeling framework that can incorporate consistent hydrate thermodynamics into descriptions of multiphase mixtures, and provide mechanistic understanding of the nonequilibrium thermodynamic control of hydrate growth on a macroscopic gas–liquid interface. Such model would help address important questions of hydrate formation in a multiphase environment, including seafloor crater formation by hydrate-controlled gas expulsion [Andreassen et al., 2017], the fate of hydrate-crusted bubbles ascending in the water column [Skarke et al., 2014; Warzinski et al., 2014; Wang et al., 2016] and the stability of hydrate within seafloor sediments under a changing climate [Ruppel and Kessler, 2017].

1.2 Phase-field methods

Phase-field modeling is a mathematical framework well suited to describe systems out of thermodynamic equilibrium [Bray, 1994; Anderson et al., 1998]. First introduced in the context of solidification and phase transitions [Cahn and Hilliard, 1958], it has since been adopted in the field of multiphase flow [Lowengrub and Truskinovsky, 1998; Folch et al., 1999a,b; Jacqmin, 1999; Hernández-Machado et al., 2003; Sun and Beckermann, 2010; Cueto-Felgueroso and Peraire, 2008; Gomez et al., 2010; Cueto-Felgueroso and Juanes, 2012; Fu, X. et al., 2016, 2017]. The phase-field approach is built upon a mathematical description of the free energy of the system. A phase variable, denoted $\phi_\alpha \in [0,1]$, is chosen to represent the volume fraction of the phase α at any given point in the domain. Under this framework, the fluid interface is naturally described as a diffuse profile of ϕ_α, a feature that facilitates thermodynamic consistency with the physical system, and leads to robust computational schemes [Liu et al., 2015; Gomez and van der Zee, 2015].

In classical thermodynamics simulators, the process of constructing phase diagrams based on energy descriptions is often referred to as Gibbs free energy minimization, where the equilibrium states along with some undetermined parameters are solved for through an iterative optimization procedure, constrained by experimental measurements [Baker et al., 1982; Ballard, A. L. and Sloan, 2004; Michelsen and Mollerup, 2007]. A convenient approach to thermodynamic modeling in the phase-field framework is to derive the Gibbs free energy of multiphase, multicomponent mixtures by blending individual phase free energies. This idea has been adopted in many phase-field models, in the context of alloy solidification [Nestler et al., 2000], liquid phase separation [Tegze et al., 2005] and hydrate formation in an aqueous solution (not on an interface) [Svandal et al., 2006, 2009]. The main advantage of a phase-blended free energy is that its convex hull can be straightforwardly identified through common-tangent constructions [van der Waals, 1894; Clerk-Maxwell, 1875; Rowlinson, 1979], simplifying equilibrium calculations and the derivation of conservation laws for the multiphase system.

In this work, we design a Gibbs free energy functional for methane–water mixtures under isobaric conditions that can be readily incorporated in phase-field models to study macroscopic interfacial processes. Our energy definition is thermodynamically consistent while numerically tractable, as it describes the phenomenological *nonequilibrium* dynamics of the hydrate system at macroscopic scale, while still predicting the correct thermodynamic *equilibrium*.

1.3 Hydrate phase diagram through a simplified Gibbs free energy

The equilibrium phase diagram is calculated through a simplified Gibbs free energy. In its minimal form, the system we study consists of three phases—methane-rich gas (V), methane-poor liquid (L_w) and hydrate (H)—and two components—CH_4 and H_2O. We denote by ϕ_α the volumetric fractions of phase α, where $\alpha = g, l, s$ refers to the vapor, liquid and hydrate phase, respectively. At any given point in the domain they satisfy: $\phi_g + \phi_l + \phi_s \equiv 1$. The system is also characterized by the pointwise methane mass fraction: $\chi = m_{\mathrm{CH_4}}/(m_{\mathrm{CH_4}} + m_{\mathrm{H_2O}})$, or by the molar fraction: $C = n_{\mathrm{CH_4}}/(n_{\mathrm{CH_4}} + n_{\mathrm{H_2O}})$. The two quantities are related by: $\chi = M_{\mathrm{CH_4}}C/(M_{\mathrm{CH_4}}C + M_{\mathrm{H_2O}}(1-C))$, where $M_{\mathrm{CH_4}} = 16$g/mol and $M_{\mathrm{H_2O}} = 18$g/mol are molar masses. Because the molar masses of the two components are similar, we can approximate $C \approx \chi$.

An isobaric phase diagram describes the equilibrium phase behavior of the system in temperature (T) and composition (χ) space at a fixed pressure; the T–χ phase diagram is discussed in detail in [Huo et al., 2003; Sloan et al., 2010] and shown here in Fig. 1(b). We focus on phase behavior above the freezing point temperature, where pure water ice does not form (Fig. 1b, red-boxed region). This region exhibits four key features: (1) a boiling point temperature T^B, above which only vapor (V) exists; (2) a triple point temperature T^T, where three phases coexist; (3) above T^T, a two-phase region of L_w–V coexistence; and (4) below T^T and above freezing, a hydrate-forming region (H) where either H-V or L-H equilibrium occurs.

For a given phase α at a fixed pressure, we formulate its corresponding Gibbs free energy, denoted f_α, as a function of χ and T. We use Wilson's model for the liquid and gas phases [Wilson, 1964], and a parabolic form for the solid phase [Nestler et al., 2000; Moelans, 2011; Cogswell and Carter, 2011]:

$$\begin{aligned} f_l(\chi, T) =& \omega_{\text{mix}}\{\chi \log(\chi) - (1-\chi)\log(1 - a_l(T)\chi) \\ & - \chi \log(1 - b_l(1-\chi)) + f_{l0}\}, \qquad (1) \\ f_g(\chi, T) =& \omega_{\text{mix}}\{\chi \log(\chi) - (1-\chi)\log(1 - a_g\chi) \\ & - \chi \log(1 - b_g(T)(1-\chi)) + f_{g0}\}, \qquad (2) \\ f_s(\chi, T) =& \omega_{\text{mix}}\left\{a_s(T)(\chi - \chi_s)^2 + b_s(T) + f_{s0}\right\}, \qquad (3) \end{aligned}$$

where ω_{mix} [J/cm^3] is a characteristic energy density. We account for nonlinear temperature dependence of f_α as suggested by [Wilson, 1964] for gas and liquid [Eqs. (1)–(2)], and as suggested by the solidification literature [Nestler et al., 2000; Moelans, 2011; Cogswell and Carter, 2011] for the solid phase [Eq. (3)]: $a_l = a_{l0}/(T/T_c)^4$, $b_g = b_{g0}/(T/T_c)^2$, $a_s = a_{s0}(T/T_c)$ and $b_s = b_{s0}(T/T_c)$, where $T_c = 1$K is the scaling temperature.

For a given phase pair α and β, the equilibrium composition of each phase, $\chi_\alpha^{\alpha\beta}$ and $\chi_\beta^{\alpha\beta}$, are obtained through the common tangent construction [van der Waals, 1894; Clerk-Maxwell, 1875; Rowlinson, 1979], where we solve the system of two equations: $f'_\alpha(\chi_\alpha^{\alpha\beta}) = f'_\beta(\chi_\beta^{\alpha\beta})$ and $f_\alpha(\chi_\alpha^{\alpha\beta}) - f_\beta(\chi_\beta^{\alpha\beta}) = (\chi_\alpha^{\alpha\beta} - \chi_\beta^{\alpha\beta})f'_\alpha(\chi_\alpha^{\alpha\beta})$. In a three-phase system, the calculation is performed three times. Using the parameters given in Table 1 (for pressure P =5MPa), Fig. 2(a) illustrates free energy

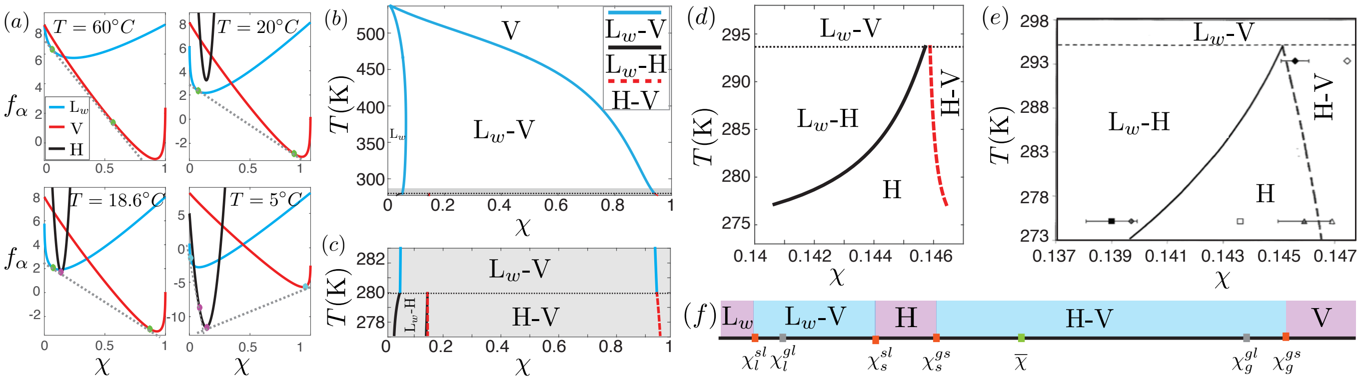

Figure 2. (a) Gibbs free energy of all phases at various temperatures. Green and red dots: equilibrium compositions; dashed grey lines: common tangents. At 5MPa, (b) analytically calculated T–χ phase diagram; (c) enlarged version of the shaded grey area in (b); At 30MPa, focusing on the hydrate-forming region, (d) analytically calculated T–χ phase diagram; (e) T–χ phase diagram from experiments adapted from [Huo et al., 2003]. Dashed line marks T^T in all figures. (f) The division of the χ axis into five phase regions by four equilibrium points (orange), not drawn to scale. The grey points correspond to gas–liquid equilibrium, which are not feasible under hydrate-forming scenarios.

Table 1. Parameters used for Gibbs free energy calculations, with $a_g = 1, b_l = 1, f_{g0} = 20$ and $f_{l0} = -20$.

P	b_{g0}	a_{l0}	a_{s0}	χ_s	b_{s0}	f_{s0}
5MPa	-9.5×10^{10}	-9.5×10^{10}	350	0.147	1.13	-42
30MPa	-1×10^{9}	-1×10^{9}	1200	0.146	0.65	-40

curves and their corresponding feasible tangent constructions at four different temperatures. At the triple-point temperature $T^T = 18.6$°C, the dashed line is tangent to all three curves. Above T^T, at $T = 20, 60$°C, hydrate does not form and gas–liquid equilibrium is favored, yielding two equilibrium compositions χ_l^{gl} and χ_g^{gl}. Below T^T, at $T = 5$°C, hydrate can readily form and the equilibrium is defined by four composition values (from left to right): χ_l^{ls}, χ_s^{ls}, χ_s^{sg} and χ_g^{sg}, which divide the χ axis into five different equilibrium scenarios [Fig. 2(f)].

Based on the calibrated parameters in Table 1, here we calculate equilibrium compositions for a wide range of temperatures (increment of 0.1K) and plot the results on a T–χ plane [Fig. 2(b)-(e)]. At $P = 5$MPa, the calculated phase diagram [Fig. 2(b)-(c)] agrees well with that obtained from experimental measurements and thermodynamic simulators in [Huo et al., 2003; Sloan et al., 2010] [Fig. 1(b)]. Our results also correctly capture the triple point $T^T = 280$K and the boiling point $T^B = 537.15$K. At $P = 30$MPa, we focus our comparison with experiments on the hydrate-forming region, where χ is expected to be equal to 0.148, based on methane hydrate stoichiometry ($CH_4 \cdot 5.75H_2O$), but instead Raman spectroscopy measurements and thermodynamic simulators have demonstrated that nonstoichiometry methane concentrations are favored [Huo et al., 2003; Sloan et al., 2010]. For instance, at $P = 30$MPa and $T \approx 277K$, $\chi_s^{sl} \approx 0.141$ and $\chi_s^{sg} \approx 0.1465$. In a T–χ phase diagram, such nonstoichiometry effects are evidenced by a separation between the L$_w$–H and H–V phase boundaries [Fig. 2(e)], which is well captured by our model [Fig. 2(d)]. In the context of hydrate growth on a gas–liquid interface, the nonstoichiometry effect indicates that hydrate that grows into a methane-rich gas phase may have higher methane concentration than hydrate that grows into a methane-poor liquid phase.

1.4 Nonequilibrium dynamics

The nonequilibrium dynamics is studied using phase-field modeling. We define $\boldsymbol{\phi} = [\phi_g, \phi_l, \phi_s]$. Under the phase-field framework, the f_α's are incorporated into the total free energy $F(\chi, \boldsymbol{\phi}, T)$, which also considers the energetic interactions between phases, and is composed of the bulk free energy f_0 and the interfacial energy (gradient squared terms):

$$\begin{aligned} F = \int_V \Big[& f_0(\chi, \boldsymbol{\phi}, T) + \epsilon_c^2(T)|\nabla\chi|^2 \\ & + \epsilon_{gl}^2(T)\nabla\phi_g \cdot \nabla\phi_l + \epsilon_{gs}^2(T)\nabla\phi_g \cdot \nabla\phi_s \\ & + \epsilon_{sl}^2(T)\nabla\phi_s \cdot \nabla\phi_l + \epsilon_g^2(T)|\nabla\phi_g|^2 \\ & + \epsilon_l^2(T)|\nabla\phi_l|^2 + \epsilon_s^2(T)|\nabla\phi_s|^2 \Big] dV. \end{aligned} \tag{4}$$

The bulk free energy, $f_0(\chi, \boldsymbol{\phi}, T)$, is made of two parts: $f_0 = \omega_{\text{mix}}\big\{G_g(\boldsymbol{\phi})f_g(\chi, T) + G_l(\boldsymbol{\phi})f_l(\chi, T) + G_s(\boldsymbol{\phi})f_s(\chi, T)\big\} + \omega_{gl}\phi_g^2\phi_l^2 + \omega_{gs}\phi_g^2\phi_s^2 + \omega_{sl}\phi_s^2\phi_l^2$. The blending functions $G_\alpha(\boldsymbol{\phi})$ for a three-phase system are taken from [Folch and Plapp, 2005] as: $G_\alpha(\boldsymbol{\phi}) = 0.25\phi_\alpha^2\{15(1-\phi_\alpha)[1+\phi_\alpha-(\phi_\beta-\phi_\gamma)^2]+\phi_\alpha(9\phi_\alpha^2-5)\}$. The evolution of the system is driven by potentials Ψ (variational derivatives of F) and described by Cahn–Hilliard and Allen–Cahn type equations:

$$\frac{\partial\chi}{\partial t} + \nabla \cdot (\mathbf{u}\chi) - R_\chi \nabla \cdot (D(\boldsymbol{\phi})\nabla\Psi_\chi) = 0, \tag{5}$$

$$\frac{\partial\phi_\alpha}{\partial t} + \mathbf{u} \cdot \nabla\phi_\alpha + R_\phi\Psi_\alpha = 0, \quad \phi_l + \phi_g + \phi_s = 1, \tag{6}$$

where R_χ is an effective rate of diffusion (the inverse of a Péclet number) and R_ϕ is an effective rate of phase transition (the inverse of a capillary number) [Fu, X. et al., 2017]. We assume simple hydrodynamics, with a Darcy-type mixture velocity, $\mathbf{u} = -[1/\mu(\boldsymbol{\phi})]\nabla p$, where p is a global fluid pressure obtained by imposing the incompressibility constraint, $\nabla \cdot \mathbf{u} = 0$, with appropriate boundary conditions. Here, $D(\boldsymbol{\phi}) = \phi_g D_g + \phi_l D_l + \phi_s D_s$ is a dimensionless mixture diffusion coefficient (where D_g, D_l and D_s are normalized by a characteristic gas-phase diffusion coefficient D_{gas}), and $\mu(\boldsymbol{\phi})$ is a similarly-defined dimensionless mixture viscosity. We adopt $D_g = 1$, $D_l = 10^{-3}$ and $D_s = 10^{-11}$ (whose relative magnitudes are consistent with experimental measurements [Witherspoon and Saraf, 1965; Peters et al., 2008] and emulate slow diffusion in liquid and extremely slow diffusion within hydrate), and $\mu_g = 1$, $\mu_l = 5$ and $\mu_s = 500$.

1.5 Hydrate growth on a quiescent gas–liquid interface

We investigate hydrate growth using the proposed model. Taking $\mathbf{u} = \mathbf{0}$, the system of four constrained PDEs in Eqs. (5)–(6) is discretized using finite elements and a monolithically-coupled implicit time integration scheme. The simulations are performed on a 1D domain ($x \in [0, 0.5]$) that is initially filled with 3/4 liquid, 1/4 gas and no hydrate [Fig. 3(a)]. Based on parameters reported in Table 1 (5MPa) and at $T = 278$K, L$_w$–H equilibrium is characterized by $\chi_l^{ls} \approx 0.010$, $\chi_s^{ls} \approx 0.13$ and H–V equilibrium is characterized by $\chi_s^{gs} \approx 0.148$, $\chi_s^{gs} \approx 0.960$. In the absence of hydrate, the L–V equilibrium is characterized by $\chi_l^{gl} \approx 0.063$, $\chi_g^{gl} \approx 0.925$. Informed by these equilibrium compositions, we perform two sets of simulations to investigate how the initial liquid methane concentration (χ_l^0) influences the growth direction and kinetics of hydrate at the gas–liquid interface [Saito et al., 2010].

In the first simulation [Fig. 3(b)], the liquid phase is initially *supersaturated* in methane, where $\chi_l^0 \approx 0.08 > \chi_l^{gl}$; in the second simulation [Fig. 3(c)], liquid phase is initially *undersaturated* in methane, where $\chi_l^0 \approx 0.005 < \chi_l^{gl}$. In both simulations, the gas phase is initialized with $\chi_g^0 = 0.93$, and the domain-averaged concentration is $\overline{\chi} = 0.25$ and 0.19, respectively [Fig. 2(f), green dot]. This indicates that, at equilibrium, we should expect H–V coexistence in both simulations.

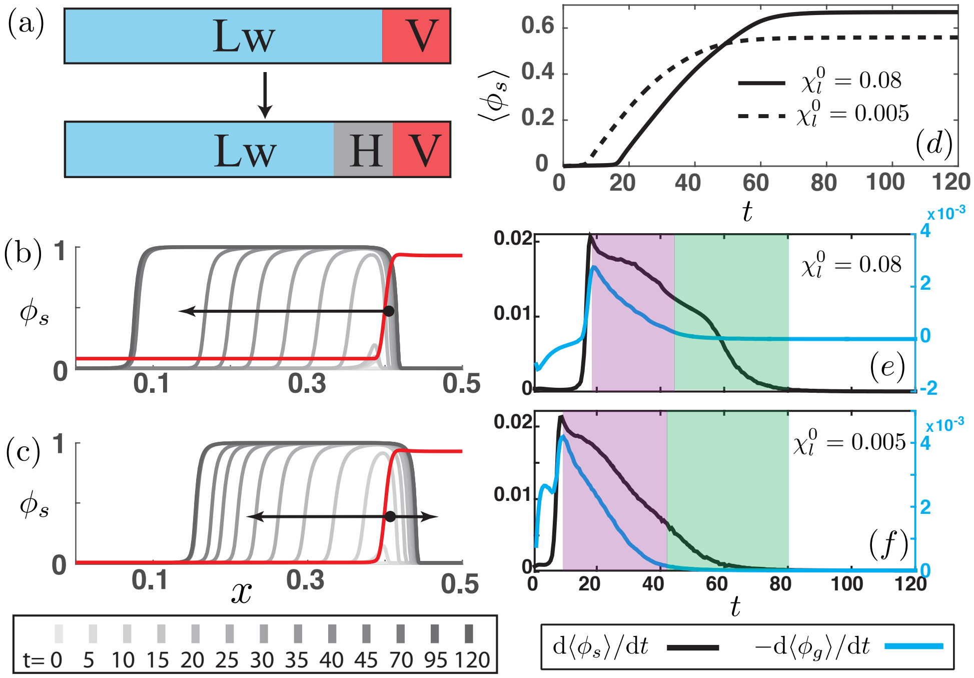

Figure 3. (a) Schematic illustrating hydrate growth on a liquid–gas interface. Simulated profiles of ϕ_s at different times (grey scale) and initial profile of χ (red) for (b) initially supersaturated liquid and (c) initially undersaturated liquid. Black arrow points to growth direction and the black dot marks the position of initial gas–liquid interface. (d) Domain-integrated ϕ_s over time. (e-f) Domain integrated hydrate growth rate (black) and gas consumption rate (blue) as a function of time, with gas–sustained (purple) and liquid–sustained (green) stages of hydrate growth.

1.5.1 Growth direction

Our simulations demonstrate that the initial liquid methane concentration determines the direction of hydrate growth at a gas–liquid interface. When liquid is initially supersaturated, our model predicts that hydrate grows predominantly towards the liquid phase [Fig. 3(b)], in agreement with experimental observations [Taylor et al., 2007]. When the liquid is initially undersaturated, the hydrate layer thickens into both the liquid and gas phases [Fig. 3(c)], consuming a significant amount of gas in order to sustain hydrate formation. In the context of hydrate formation around a methane gas bubble, these results could explain why some hydrate-armored bubbles buckle due to depletion of gas pressure inside the bubble as hydrate forms in undersaturated water [Chen et al., 2014; Waite et al., 2017], while some hydrate-coated bubbles can stay inflated when hydrate forms in supersaturated conditions [Warzinski et al., 2014].

1.5.2 Two stages of kinetic growth

By tracking the domain-averaged hydrate fraction $\langle \phi_s \rangle$ over time for both simulations [Fig. 3(d)], we observe that hydrate thickens at a decreasing growth rate that eventually becomes close to zero [Fig. 3(e)-(f), black curve], which agrees well with experimental studies [Taylor et al., 2007]. As a result of this hydrate-formation shutdown, the domain arrives at a *quasi*-steady configuration of three-phase coexistence [Fig. 3(a), bottom], which is not predicted by equilibrium calculations [Fig. 2(f), green dot] that instead predict H–V coexistence at steady state. The nonequilibrium steady state has been understood as a diffusion-limited phenomenon, where the extremely slow diffusion within the hydrate phase can severely hinder the continued growth of hydrate into the liquid phase [Abe et al., 2016; Svandal et al., 2009; Taylor et al., 2007]. By comparing hydrate growth rate against gas consumption rate [Fig. 3(e)-(f)] and analyzing details of composition profiles, here, we provide mechanistic insights into two distinct stages of this diffusion-limited growth. In the first stage [purple in Fig. 3(e)-(f)], gas is consumed to supply the methane needed for hydrate formation. During this stage, the liquid methane concentration, χ_l, remains constant if it is initially supersaturated, or increases if initially undersaturated. The hydrate phase methane concentration, χ_s, equals χ_s^{gs} (the H–V equilibrium). In the second stage, after a significant amount of hydrate has formed in between the gas and liquid, the gas–hydrate interface reaches equilibrium and hydrate growth stops on the gas side but continues into the liquid; no more gas is consumed [green in Fig. 3(e)-(f)]. During this stage, χ_l decreases towards χ_l^{ls} and χ_s also decreases towards χ_s^{sl} on the side that grows into the liquid. This second-stage growth is driven by the thermodynamically imposed compositional gradient within the hydrate phase [Huo et al., 2003], and is therefore limited by the extremely slow diffusion within the hydrate.

1.6 Persistent gas conduits in hydrate-bearing sediments

Gas conduits have been widely observed in field surveys [Suess et al., 1999; Liu and Flemings, 2006; Bangs et al., 2011], although their formation mechanisms are not well understood. Here, we demonstrate that nonequilibrium hydrate growth on moving gas–liquid interfaces provides a plausible explanation for the formation of these gas conduits. We solve Eqs. (5)–(6) in a rectangular domain, with upward flow sustained by an imposed pressure gradient ($p_2 > p_1$), emulating buoyancy-driven gas migration in seafloor sediments (Fig. 4). We describe hydrate as a highly viscous fluid (viscosity contrast $\mu_s/\mu_g = 500$) that exerts significant resistance to the gas movement upon formation at the gas–liquid interface.

We show two simulations, where the only difference is the magnitude of the imposed pressure difference, $\Delta p = p_2 - p_1$: the pressure difference in the first simulation is twice that of the second simulation. In the first simulation [Fig. 4(a) in this document], upward gas movement is fast enough to overcome the restraint of the hydrate layer, leading to continued elongation of the gas conduit. In the second simulation [Fig. 4(b) in this document], gas moves relatively slowly, and the elongation of the gas conduit is hindered and eventually arrested by hydrate formation at the interface. The conduit becomes sealed off at the top, and the shape persists due to the extremely slow diffusion within the hydrate phase, leading to a long-lived nonequilibrium configuration.

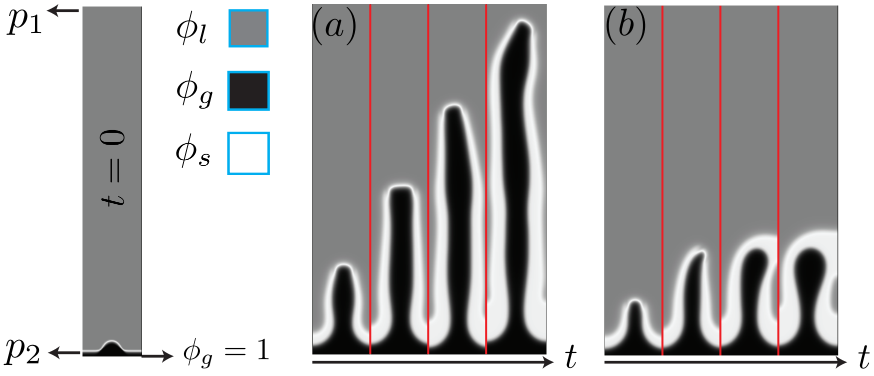

Figure 4. Simulations illustrating hydrate-encased gas conduits forming in initially undersaturated liquid ($\chi_l^0 = 0.005 < \chi_l^{gl}$). Simulation (a) corresponds to a pressure difference driving the flow that is twice that of simulation (b).

1.7 Conclusions

In summary, we develop a continuum-scale phase-field model to study methane hydrate systems far from thermodynamic equilibrium. We design the bulk Gibbs free energy to describe thermodynamic equilibrium, which recovers the isobaric temperature–composition phase diagram from experimental studies. We then incorporate this free energy into a phase-field model to study formation dynamics of hydrate on a gas–liquid interface. Our model predicts that initial aqueous concentration exerts powerful control on the growth direction of hydrate, where hydrate grows dominantly into liquid if liquid is initially at/over saturation, and grows into both liquid and gas if liquid is initially undersaturated. This result has significant implications to the long-standing puzzle of why some hydrate-coated gas bubbles collapse due to hydrate formation [Chen et al., 2014; Waite et al., 2017] and some do not [Warzinski et al., 2014]. Our model correctly recovers the diffusion-limited kinetics of hydrate growth as measured in experiments. By tracking the source of methane supply during hydrate formation, we further demonstrate that hydrate growth is in fact two-staged; in the first stage, methane needed for hydrate formation is dominantly supplied from the gas phase; in the second stage, hydrate growth continues into the liquid phase without consuming any gas. This could explain the occurrence of persistent gas conduits in some hydrate-bearing sediments [Suess et al., 1999; Liu and Flemings, 2006; Bangs et al., 2011] and other nonequilibrium phenomena commonly observed in natural methane hydrate systems.

2 Laboratory observations of the evolution and rise rate of bubbles with and without hydrate shells

2.1 Introduction

Methane hydrates represent a vast pool of methane that accounts for 1/6 or more of the world's mobile, near surface carbon [Ruppel and Kessler, 2017]. Though considered a potent greenhouse gas [IPCC, 2001], ∼99% of the world's gas hydrates exist in the marine environment [Ruppel, 2015], and methane released in seafloor sediment is thought to be largely consumed by microbes in the sediment [Reeburgh, 2007] and water column [Valentine et al., 2001; Mau et al., 2007] before reaching the atmosphere [Ruppel and Kessler, 2017]. Though microbial consumption of methane in the water column reduces methane's atmospheric contribution, there is still an environmental cost: the aerobic microbial process consumes dissolved oxygen and produces carbon dioxide, depleting the water column of oxygen while increasing the acidity [Valentine et al., 2001]. An increasing awareness of the large number, distribution [Skarke et al., 2014; Greinert et al., 2010b; Westbrook et al., 2009] and longevity [Berndt et al., 2014] of seafloor methane seeps, some of which have been tied to dissociating methane hydrate [Skarke et al., 2014; Greinert et al., 2010b; Westbrook et al., 2009; Berndt et al., 2014] has motivated research into the fate of methane in the water column.

Quantifying the extent and water depths at which oxygen depletion and acidification are likely to be significant requires understanding the fate of methane in bubbles emitted from the seafloor. As bubbles rise, methane diffuses from the bubbles and becomes the dissolved-phase methane accessible to the microbial community [Mogollón et al., 2011]. The rate at which methane diffuses from a bubble depends on several parameters, including bubble size, rise velocity and the rate of diffusion through the bubble surface [McGinnis et al., 2006]. The bubble surface itself is variable, because bubbles entering the water column below ∼300 m depth in cold water environments [Ruppel and Kessler, 2017], or below ∼500 m depth in warmer mid- to low-latitude waters [Ruppel and Kessler, 2017; Zhang, 2003], exist within methane gas hydrate stability conditions and have been observed to form hydrate shells [Rehder et al., 2002; Wang et al., 2016]. Hydrate-coated bubbles may dissolve more slowly than their hydrate-free counterparts [Rehder et al., 2002], thereby changing the methane release profile of a rising bubble.

To better understand the likely depth profile of gas concentrations with depth left behind by a rising bubble, key parameters controlling the rate at which gas dissolves out of a bubble were investigated. In particular, relationships between bubble size, surface coating (hydrate shell or hydrate free) and rise rate were studied in a laboratory flow loop with a large transparent observation chamber. Air, xenon and xenon-hydrate coated bubbles were analyzed in this work.

2.2 Apparatus

To capture and study gas bubbles rising through water, a flow loop has been constructed using the "capture cone" elements described by Maini and Bishnoi [1981] and Warzinski et al. [2014]. The cone is housed within a clear acrylic cylinder that acts as a pressure chamber (Fig. 5, left). The cone's cross sectional area increases toward the bottom of the chamber, so water pumped down through the cone smoothly transitions from higher velocity at the cone's top, to lower velocity at the bottom. A bubble released into the cone from below will rise until reaching a position in the cone at which the downward water velocity balances the bubble's upward rise velocity. The position of the bubble in the cone is tracked with a camera referenced to rulers attached to the front and back of the pressure chamber (Fig. 5, left).

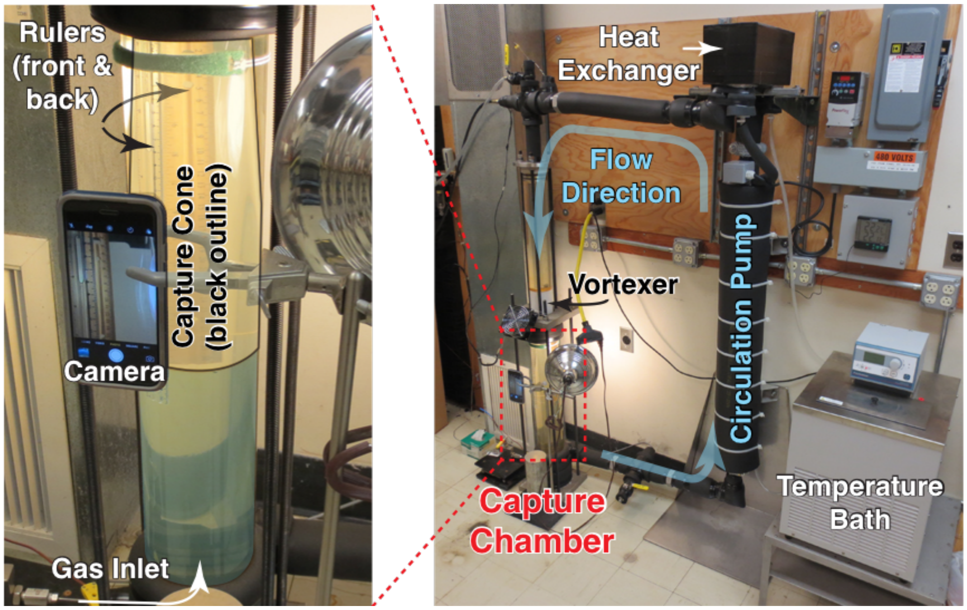

Figure 5. Flow loop apparatus for investigating bubbles rising in water. (Left) A gas bubble released from the gas line at the base of the system rises into the capture cone until the downward water velocity matches the bubble's rise velocity. A camera records the bubble's location with respect to two rulers, one in front, and one behind the acrylic outer chamber. (Right) A variable- speed circulation pump controls water flow rates. A temperature bath controls the flow loop temperature by pumping water around the outside of the circulation pump and through the heat exchanger. Syringe pumps (not shown) control the water pressure and gas injection.

Water flow through the capture cone is controlled by a variable speed circulation pump (Fig. 5, right). The flow rate can be tuned by adjusting the frequency of the voltage driving the pump. The circulating water pressure is controlled by a syringe pump connected to the flow loop just above the vertical acrylic chambers. A second syringe pump is used to inject gas at the base of the capture chamber, and single-bubble injections are accomplished by manually opening and closing a ball valve in the gas line near the base of the capture chamber. To investigate bubbles in the 1.5–10 mm diameter range, the gas inlet is a 1/16-in pipe (1.59 mm inner diameter).

Flow loop temperature is controlled with a circulating temperature bath (Fig. 5, lower right). Chilled water is pumped from the bath through flexible tubing coiled around the length of the flow loop's circulating pump, then through a sandwich style copper heat exchanger, mounted atop the circulating pump, before returning to the cooling bath. The heat exchanger forces circulating flow loop water through a series of plates cooled by the cooling water, and is responsible for the bulk of the temperature control in the flow loop. Because the flow loop is constructed primarily of standard 1-in pipe and other metal components, all non-acrylic components of the flow loop are encased in insulation (black wrapping in Fig. 5, right). The flow loop water is typically cooled to 9.7°C for hydrate- formation experiments, but even for "room temperature" tests near 25°C, the cooling system is required to counteract frictional heating within the flow loop's circulating pump and flow lines.

Flow loop environmental data, such as flow rate, temperature, water and gas pressure, are recorded digitally. The flow rate is measured with a calibrated turbine-style flow meter mounted along the top horizontal leg of the loop. Water temperature is measured with two thermocouples, one inserted into the circulating water from above the acrylic chambers, and one inserted at the base of the capture cone chamber. With the circulating pump running, the two temperature readings become equal in less than a minute. Pressure is measured in the lower horizontal leg of the flow loop in the return line to the circulating pump. Syringe pump data, including volume, pressure and injection rates, are recorded in a separate digital file.

Bubbles are analyzed based on recorded imagery from the camera mounted in front of the capture cone. Rulers mounted in front of and behind the acrylic outer chamber are used to quantify bubble size and height within the cone.

2.3 Methods

This study reports on bubbles of air, xenon gas, and xenon hydrate-coated bubbles in de-aerated tap water. Xenon is chosen as the hydrate-forming gas instead of methane because, though they both form the sI hydrate structure, xenon hydrate forms at pressure and temperature conditions (Fig. 6) that are modest enough to be recreated in an optically-clear chamber. The hydrate formation technique is described below, along with the methodology for two types of experiments: captured bubble tests, ideal for observations of a single bubble's evolution over time; and free-rise tests, which are better suited for quantifying bubble rise rates. Procedures for obtaining bubble locations, size and shape from the available imagery are presented at the end of this section along with estimates for the primary sources of error.

2.3.1 Hydrate formation technique

Though xenon hydrate is stable at the ∼1 MPa, 9.7°C test conditions used here, the dissolved xenon concentration in the circulating water must be sufficiently high before hydrate formation at the bubble surface can outpace the dissolution of gas into the circulating water. This behavior has been observed in previous flow loop studies [Maini and Bishnoi, 1981; Warzinski et al., 2014; Chen et al., 2014]. Like methane, xenon forms a structure I hydrate [Sloan and Koh, 2008], but compared to methane hydrate, relatively little is known about the solubility of xenon in the presence of hydrate. Without a known target xenon concentration, pulses of xenon bubbles were simply injected into the flow loop and allowed to dissolve until hydrate formation was observed on the bubbles. Once these first hydrate-forming bubbles dissolved, a single xenon bubble was injected and the circulation pump was tuned to hold the bubble level with the camera, near the top of the capture cone. As the captured bubble dissolved over time, the circulating water pump speed was reduced to maintain the hydrate-coated bubble's position in the capture cone. Movies were taken periodically to track the bubble's shape over time.

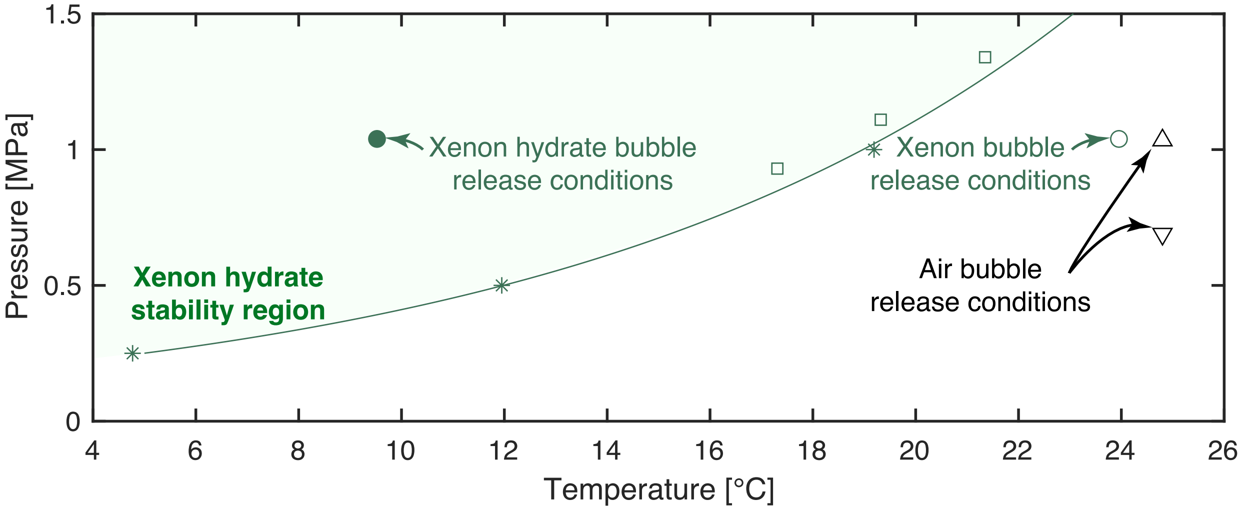

Figure 6. Pressure and temperature conditions for the flow loop tests. Shaded region indicates the elevated pressures and reduced temperatures required for xenon hydrate formation. Phase boundary is an exponential fit to the data compiled by Sloan and Koh [2008] (green stars). Green squares are phase boundary measurements by Ohgaki et al. [2000]. Throughout this report, air results are plotted as black triangles facing upward for 1 MPa measurements, and downward for 0.7 MPa measurements. Open green circles represent hydrate-free xenon bubbles, and solid green circles represent hydrate-coated bubbles.

2.3.2 Bubble capture

Capturing a bubble requires limiting both the vertical and horizontal motion of the bubble. Vertical motion can be balanced in the capture cone by tuning the water flow rate and taking advantage of the cone's shape. The cone provides a gentle velocity gradient as water passes through the narrow upper opening of the cone (~20 cm^2), slowing as the water moves through the ever-widening cone until reaching the cone's bottom (~60 cm^2). The factor of ~3 increase in cross-sectional area imparts a factor of 3 drop in velocity over the cone's 28 cm height, making it relatively easy to tune the circulating flow rate so a bubble of interest can be captured at a given position in the cone. Typical flow rates are 300–600 cc/s (4.75–9.5 gal/min).

To restrict lateral bubble motion and prevent bubble interactions with the flow loop walls, the ideal water velocity profile should be slow along the flow loop's central axis, and faster away from the central axis (Fig. 7). Bubbles rising in such an environment tend to slide toward the flow loop axis, out of the path of the fastest-moving water. The flow loop used here employs a vortexer developed at the University of New Hampshire (white cylinder atop the capture chamber in Fig. 5). The vortexer is a plastic, 3D printed cylinder supporting a helix within the cylinder. Circulating water passes through the vortexer's helix, which establishes a rotation to the flow. This rotation preferentially pushes dense water away from the flow loop's central axis, helping to restrict the low density gas bubbles to the near-axis region. A cloud of injected bubbles demonstrates the overall bubble motion is to rise along the central axis and fall when pushed away from the central axis by other bubbles, implying the vortexer establishes a water velocity profile similar to the idealized case in Fig. 7.

Because the vertical water velocity profile is shaped conceptually as shown in Fig. 7, rather than being uniform across a given surface, the velocity along the central axis that balances the bubble's rise is not known precisely. Consequently, the capture technique is used to observe bubble evolution over time, rather than to quantify rise rates in absolute terms.

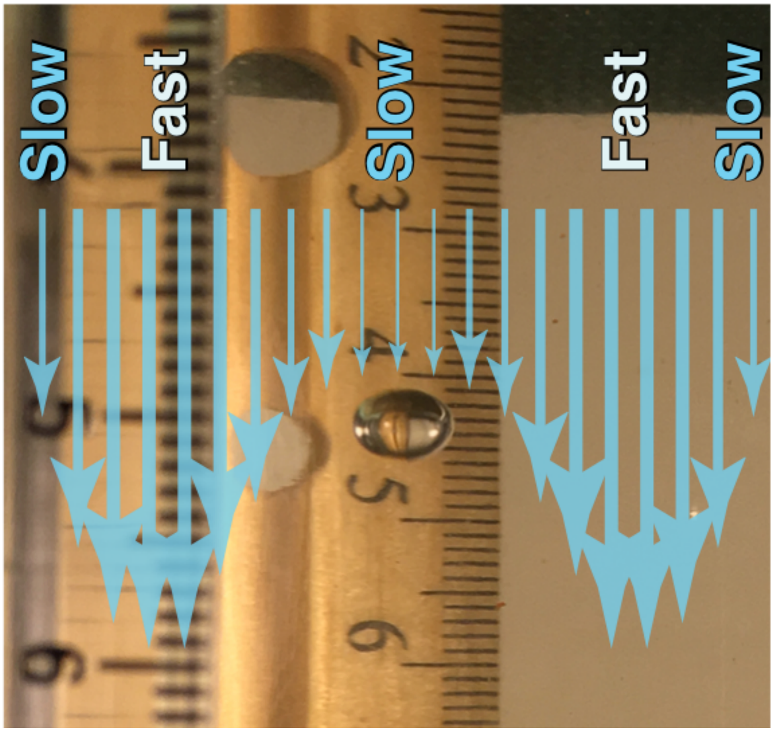

Figure 7. Xenon gas bubble captured in the flow loop capture cone. An idealized water velocity profile is indicated by the downward arrows. To retain a bubble near the central axis, the water should be slow near the axis, increase to a peak velocity away from the axis before boundary effects at the chamber walls reduce the water velocity. This profile is accomplished here with a vortexer mounted above the capture cone (see Fig. 5).

2.3.3 Free rise

To quantify bubble rise rates, individual bubbles are released when the flow loop water is stationary and the temperature is held at the conditions shown in Fig. 6. The bubble rise is tracked at 240 frames per second, and frames are noted when the bubble passes six ruler locations (Fig. 8). As discussed in the "Error analysis" section, the bubble is assumed to travel up the flow loop's central axis. The assumed bubble positions are calculated for each ruler location in Fig. 8 (left) by applying Snell's law to the acrylic interfaces and water layers (see Fig. 9). The rise rate is taken as the slope of the linear fit through the location versus time data (Fig. 8).

2.3.4 Bubble size and shape characterization

Bubbles are assumed to be ellipsoidal in this study, so their size and shape are described by bubble height and diameter measurements made on an image of the bubble taken when the bubble is level with the camera and the front and back ruler values are equal (Fig. 8, left, 8-cm mark, location #3). Each bubble dimension is taken as the average of the measurements made using the front and

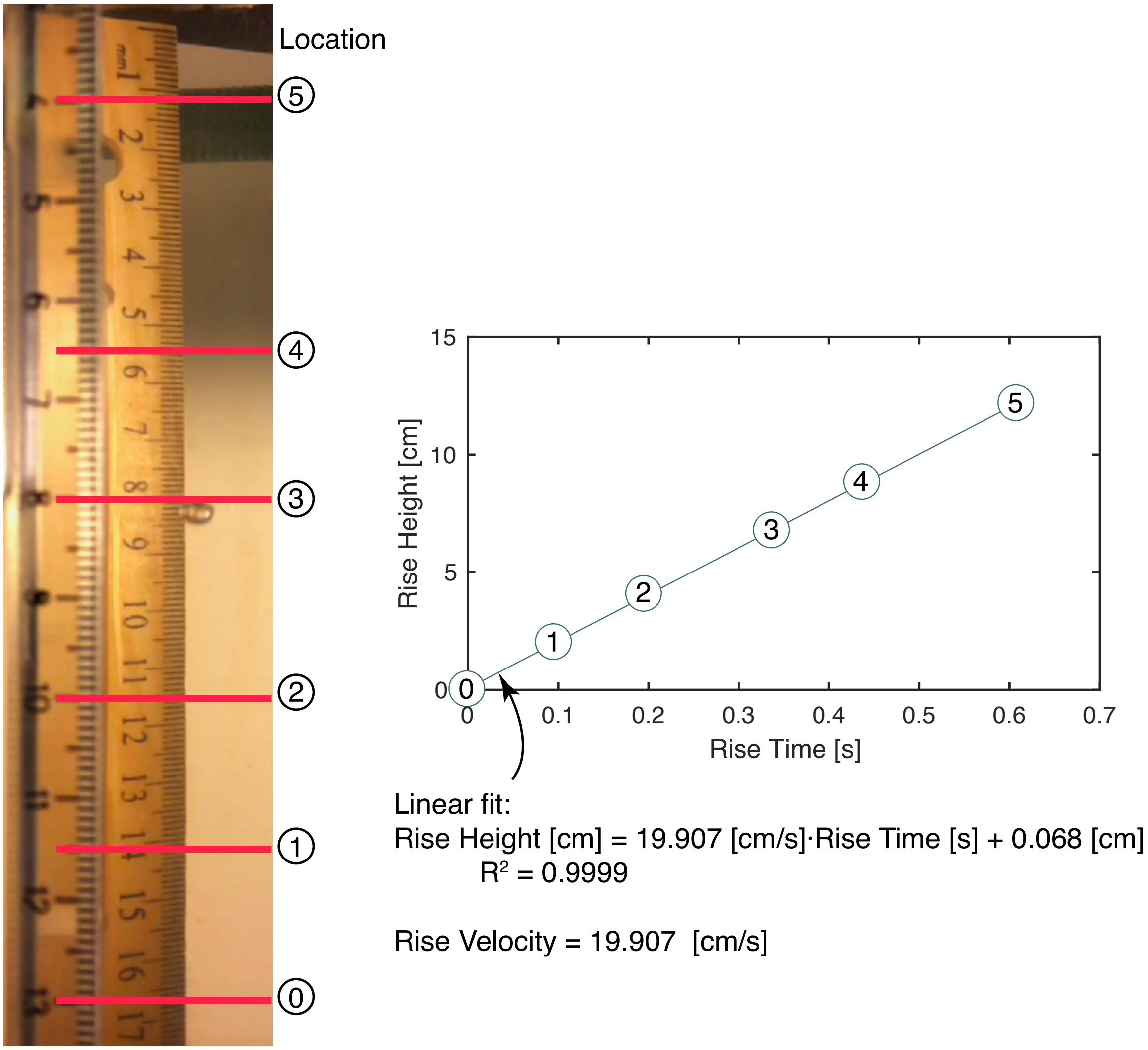

Figure 8. Free rise velocity calculation. A bubble's position is tracked at 240 frames per second as it passes the 6 locations indicated by red lines (left). Rise velocity is taken as the slope of the linear fit through the rise height versus rise time data (right). Bubble diameter and height are calculated from the bubble image as it passes the 8-cm mark, location #3 (left).

back rulers, meaning the bubble is assumed to be midway between the rulers. The uncertainty this approach creates is discussed in the "Error analysis" section.

To compare measured bubble properties with literature results, it is convenient to describe the bubble size in terms of an effective spherical diameter, d_e, which is the diameter of a sphere of the same volume as the bubble of interest. For the ellipsoidal bubble shapes assumed in this work, de is given by:

$$d_e = (d^2h)^{1/3}, \tag{7}$$

where d and h are the bubble's measured diameter and height, respectively. A second shape parameter of interest is the flatness, f:

$$f = \frac{d-h}{d}. \tag{8}$$

Both the bubble's volume, as described by its equivalent diameter, d_e, and flatness, f, play critical roles in determining a bubble's overall rise rate.

2.3.5 Error analysis

The fundamental source of error in this study is due to single vantage-point observations. With only a single camera, it is impossible to measure the "front-to-back" location of a bubble along the line of sight. A modest constraint is possible because the vortexer forces captured bubbles to remain near the central axis, and free-rise bubbles are excluded if they contact the cone walls (as determined by eye from the side of the apparatus in conjunction with the camera's bubble track). With these constraints, and knowing the top of the cone has a 2.54-cm radius, the bubble can be generally assumed to exist within 2.54 cm of the flow loop's central axis. To establish potential errors in bubble position and size, this radial constraint must be paired with the true ray paths for light passing between given points on the front and back rulers. Fig. 9 (left) is a side view schematic of the capture cone in the acrylic chamber, and combines the radial position constraint (dashed red lines) with the refracted paths of light traveling between the ruler marks used in Fig. 8 for determining free rise velocities. Because the indices of refraction, n, for the acrylic, 1.49 [Tap Plastics, 2015], and water, 1.33 [Weast et al., 1989], are similar, and the incident angles, θ, between the light rays and the chamber interfaces do not deviate significantly from 90°, the complete ray paths calculated via Snell's Law:

$$n_{\text{acryllic}} \sin \theta_{\text{acryllic}} = n_{\text{water}} \sin \theta_{\text{water}}, \tag{9}$$

show very little deviation from refraction-free straight lines. Nonetheless, because the rise velocity is calculated by assuming the bubble travels directly up the central axis of the cone, there is a $\pm 12\%$ uncertainty in the rise rate due to the possibility of the bubble traveling along either the shortest path (close to the camera) or the longest (away from the camera).

Similarly, the bubble diameter is calculated as the average between the dimensions taken from the back and front rulers, meaning the bubble is assumed to be located on the central axis of the capture cone. If the bubble's true location were 2.54 cm away from the central axis, the diameter estimates would be off by $\pm 12.5\%$.

Error in the time component of the velocity calculation is insignificant because timing is based on the camera's frame rate. An independent frame rate check performed by taking a movie of a digital timer shows the measured frame rate is within 0.5 frames per second of the assumed 240 frames per second rate. Errors in counting frames as the bubble travels between the red height marks in Fig. 8 (left) are minimized by the linear regression to the data (Fig. 8, right), which always has an $R^2 > 0.999$.

2.4 Results and discussion

Four types of observations are included in this study: 1) hydrate formation on the surface of bubbles; 2) evolution of a hydrate-coated bubble over time at constant pressure; 3) evolution of a hydrate-coated bubble during a simulated rise through the water column (decreasing pressure); and 4) bubble rise-rate measurements of air, xenon gas, and xenon-hydrate coated bubbles in still water.

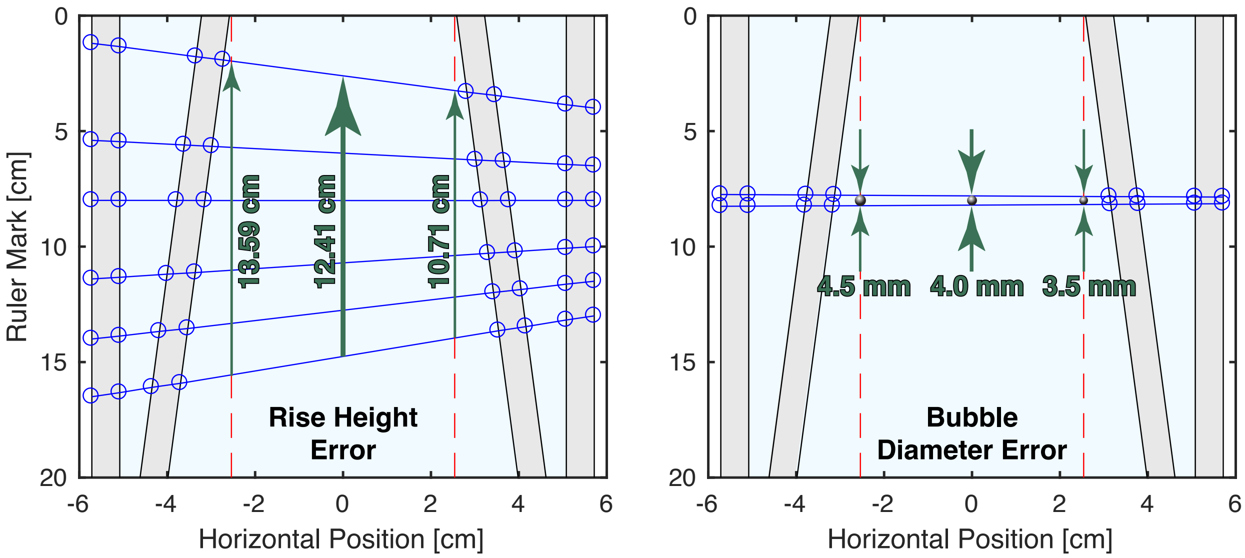

Figure 9. Measurement uncertainties in the bubble position (left) and size (right). The acrylic chamber and cone are shaded in gray, water is shaded blue. Light rays connecting the back ruler (left side of each diagram) and front ruler (right side of each diagram) are shown in solid blue line segments, with blue circles highlighting interface intersections. Light paths are calculated from Snell's Law (Eq. (9)). Bubbles are rejected if they interact with the cone walls, and are assumed to remain within 2.54 cm of the central axis (red dashed lies). The rise height uncertainty is ±12%, and the bubble size uncertainty is ±12.5%.

2.4.1 Hydrate formation on the surface of bubbles

The formation of hydrate shells on bubbles of hydrate forming gas is known to require elevated concentrations of hydrate-forming gas to already be dissolved in the flow loop water [Maini and Bishnoi, 1981; Warzinski et al., 2014; Chen et al., 2014]. The dissolved hydrate former's presence slows the rate of dissolution from the bubble, eventually slowing the dissolution enough for the hydrate- forming gas to form a hydrate shell at the bubble's surface rather than simply dissolving into the surrounding water. Thus, the first xenon bubbles released into the flow loop at 9.7°C and ∼1 MPa were hydrate-free, in spite of being well within the xenon hydrate stability field (Fig. 6). These initial bubbles had shiny, flexible surfaces and were transparent (Fig. 10A).

After several gas injection and bubble dissolution cycles, the dissolved xenon content approached 0.0168 moles/kg water, and some bubbles began forming opaque, frosty shells, even while their neighbors remained clear and seemingly hydrate free (Fig. 10A, top). A few bubbles were observed in transition between being hydrate-free and hydrate-coated, and like the initial stages of shell growth observed by Warzinski et al. [2014], the transition bubbles had clear, seemingly hydrate-free tops, and a hydrate shell on the bottom (Fig. 10B, bottom). Warzinski et al. [2014] attributed this growth pattern to the elevated concentration of dissolved gas in the turbulent, recirculating wake beneath a bubble relative to the water washing over the bubble's top. Collisions between frosted and clear bubbles did not appear to nucleate hydrate growth on the clear bubbles. Once all of the coexisting hydrate-free, hydrate-coated and combination bubbles dissolved, subsequent bubbles appeared to rapidly grow fairly uniform shells (Fig. 10C), as discussed in the next section. These rapid-formation shells had a matte gray look rather than the frosty white form observed when hydrate-free and hydrate-coated bubbles coexisted.

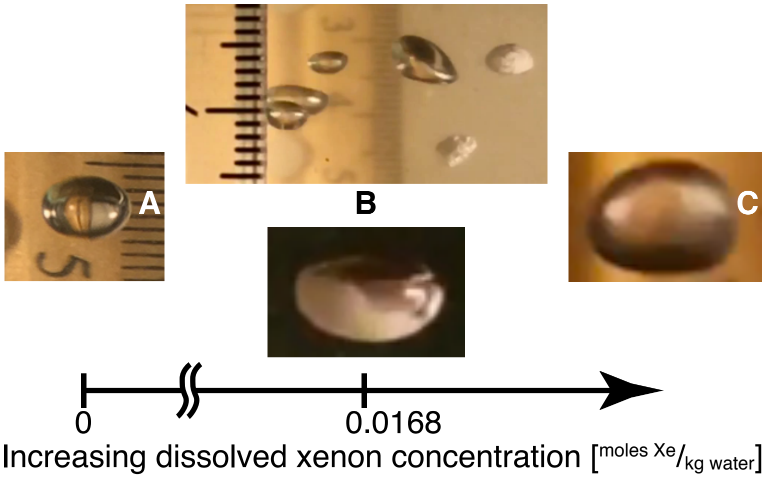

Figure 10. Bubble morphology with increasing dissolved-phase xenon content. (A) Initially shiny, transparent bubbles give way to bubbles that are (B) fully or partially coated in a white, frosty hydrate shell at 9.7°C, ∼1 MPa when the dissolved phase xenon concentration reaches 0.0168 moles Xe/kg water. (C) Subsequent bubbles form uniform, gray shells even before the bubbles themselves are observable in the chamber.

2.4.2 Evolution of a hydrate-coated bubble at constant pressure

Fig. 11 illustrates the collapse, over time, of a xenon-hydrate coated bubble at constant pressure and temperature. The bubble was initially ellipsoidal (Fig. 11, image 1), and though the bubble had a hydrate shell from the moment it rose into the capture cone, the shell was thin enough to vaguely see the brown ruler behind the bubble. The bubble's initial equivalent diameter was 4.6 mm. After only two minutes (image pair 2), the shell thickened enough to become opaque. Almost immediately, the bubble began collapsing as xenon was either consumed to thicken the hydrate shell or diffused into the circulating water. Though the top portion of the bubble acquired a dent almost immediately, this portion of the bubble remained otherwise smooth and generally unchanged for the duration of the test (upper sequence of images in Fig. 11). By comparison, the lower portion of bubble eroded significantly. An initial dent (lower image 2) broadened and deepened (lower images 3–5), eventually becoming a channel spanning the length of the bubble (lower image 6). The bubble thinned, taking on a catamaran shape with most of the remaining bubble volume existing in two sacks running along the two long sides of the bubble (lower image 7). The appearance of wrinkled or partially-collapsed hydrate-coated bubbles has also been observed for methane bubbles [Chen et al., 2014].

Over the course of the test at constant water pressure, bubble thickness and velocity decreased by ∼33%, with only a 10% decrease in diameter. The bubble appeared intact for the entire test. Observable bubbles of xenon were not released from the primary bubble, nor did the bubble observably slough off flakes of hydrate. Previous flow loop tests for methane hydrate-coated bubbles did observe flakes of hydrate being shed from bubbles [Maini and Bishnoi, 1981; Warzinski et al., 2014], though shedding was observed when the formation conditions were several MPa above the stability curve. Maini and Bishnoi [1981] note that hydrate formation was so rapid at the extremely high formation pressures for which flaking was most prominent, that stabilizing a bubble was difficult. Rather than forming a hydrate shell, the "bubble rapidly collapsed into large flakes of hydrate." For less aggressive formation pressures, hydrate was not observed to flake off bubbles

[Maini and Bishnoi, 1981]. Flaking was also observed to cease once the bubble developed a uniform shell [Warzinski et al., 2014]. As the xenon hydrate tests described in this work used only modest pressure oversteps into the hydrate stability region (<1 MPa), and the observed hydrate shells appeared uniform once the dissolved phase xenon concentration exceeded ∼0.0168 moles Xe/kg water, the absence of flaking in these tests agreed with existing observations.

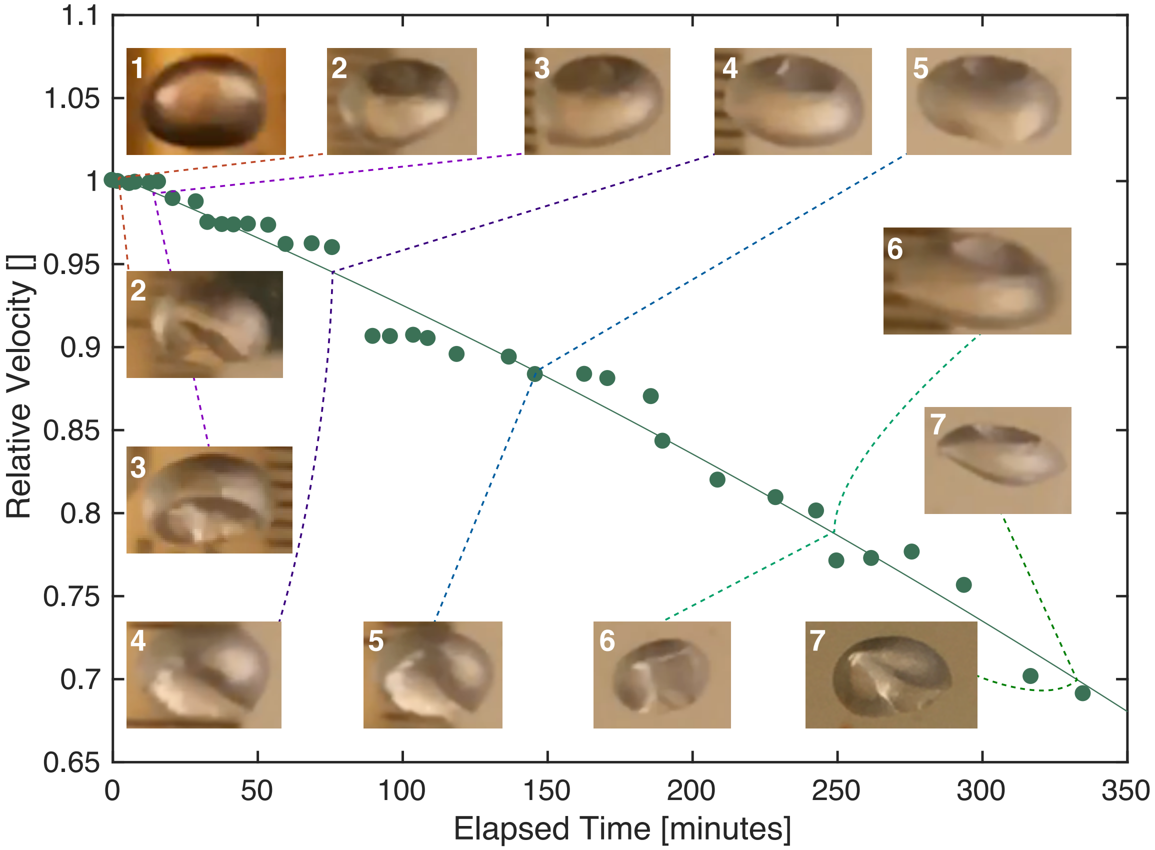

Figure 11. Evolution of a hydrate-coated bubble over time at constant pressure. The bubble shell deformed and appeared to collapse as the bubble shrank. Volume loss was greatest in the vertical direction: most of the deformation and erosion occurred on the underside of the bubble (images set below the trend of relative velocity with time). The bubble's top side acquires a dent early on, but otherwise appears to remain largely unchanged (images set above the trend of relative velocity with time). Relative to the bubble's initial rise rate, the velocity loss was nearly linear with time, accelerating only slightly over the course of the test.

2.4.3 Evolution of a hydrate-coated bubble during a simulated rise (decreasing pressure)

Fig. 12 shows the evolution of the final hydrate-coated bubble from Fig. 11 (image pair 7) as the flow loop pressure was decreased from ∼1 MPa to ∼0.3 MPa at 0.073 MPa/min. The depressurization rate was chosen to mimic the rise of a bubble traveling at the ∼12.5 cm/s calculated for the collapsed bubble at the end of the bubble evolution test. This rise rate remains an uncalibrated value due to the unknown flow velocity along the flow loop's central axis, so the depressurization rate was not likely chosen in perfect agreement with the bubble's true initial rise velocity. In Fig. 12, image 1 is the bubble as it was at the end of the evolution test, with most of the bubble volume held in two lobes on either side of the bubble's collapsed central axis. As the pressure dropped, the bubble appeared to expand as though it were a balloon being re-inflated, which has also been observed in laboratory studies of methane-hydrate coated bubbles [Chen et al., 2014]. Images 2 and 3 in Fig. 12 show expansion in the two lobes, and the lobes began reconnecting with each other on the side of the bubble facing the camera in image 4. Image 5 shows a more fully expanded bubble where the central crease through the bubble from image 1 appeared to have filled in completely. As image 6 shows, however, the bubble took on a donut shape, with one missing section (in the foreground of image 6, but hidden in the background of image 5). Bubble expansion corresponded to a rise rate increase of ~17%, in spite of the distorted shape of the bubble's upper surface.

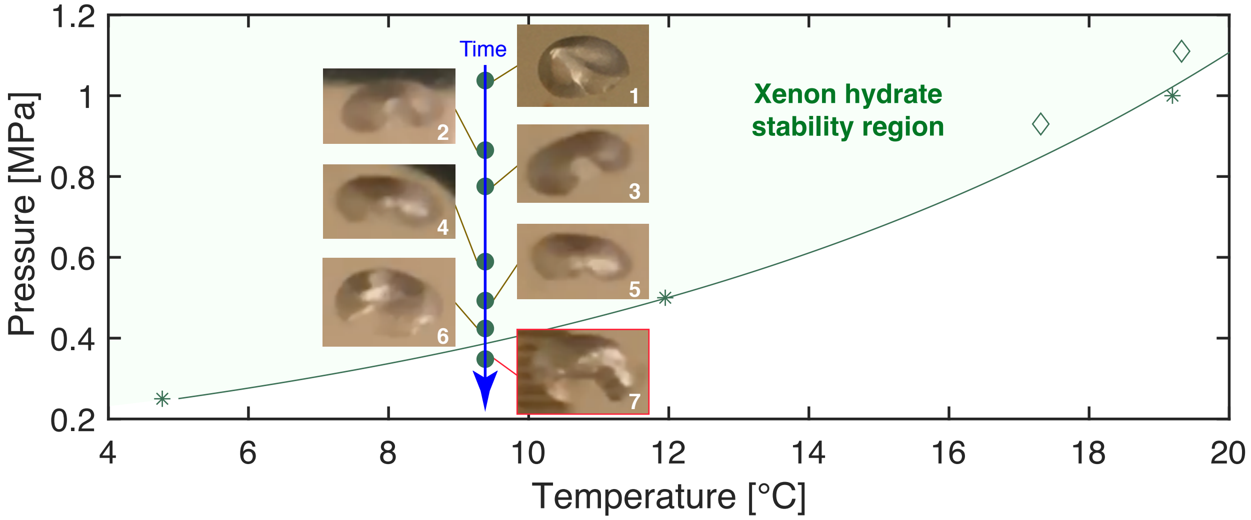

Figure 12. Evolution of a hydrate-coated bubble as pressure decreased to simulate a bubble rising at a constant 12.5 cm/s (green circles). Image 1 is taken from the final state of the bubble evolution test (image 7 in Fig. 11). During depressurization, the bubble appeared to re-inflate, with a corresponding rise rate increase. The shell appeared to remain intact throughout the expansion, persisting even when the bubble exited the hydrate stability zone (shaded green region). Phase boundary is an exponential fit to the data compiled by Sloan and Koh [2008] (green stars). Green squares are phase boundary measurements by Ohgaki et al. [2000].

As pressure dropped 0.05 MPa (~6 psi) below the xenon hydrate stability pressure, the hydrate shell persisted for at least 12 minutes. The bubble's final decay was not observed. Image 7 in Fig. 12 was the same orientation as image 5, but taken from slightly below the bubble to highlight the gap visible in the foreground of the image 6 "donut." Throughout the depressurization, and even outside the hydrate stability field, bubble expansion appeared to occur without the bubble leaking observable free xenon bubbles, or sloughing off visible flakes or pieces of the bubble shell. It is likely the thinned shell at the far side of the bubble in image 1 dissolved along the collapsed central axis. This would account for the "missing" section of the donut in images 6 and 7, and could correspond to the very thin, hardly visible portion of shell at the lowest portion of the bubble in image 6. Though the hydrate shell appeared rigid in all movies of the bubble, the shell was capable of collapsing and expanding without observably rupturing or releasing free gas at any point during the test. The water clarity did not change as the system depressurized below the hydrate stability zone, indicating the circulating water was not fully saturated with xenon during this test. Had the water been fully saturated, depressurizing out of the stability field at constant pressure would have supersaturated the fluid, caused bubbles to form in the circulating water and either made the water cloudy or created observable bubbles.

2.4.4 Rise rate observations

A series of free rise experiments were run to observe rise velocities of air, xenon gas, and xenon hydrate-coated bubbles. As bubbles rose through stationary water past the observation camera, the measured velocity of each bubble was constant (see example data in Fig. 8), suggesting each bubble reached its terminal velocity prior to entering the measurement region. Terminal rise velocities have been studied in detail for bubbles, and it is the approach of McGinnis et al. [2006] that is followed here. As McGinnis et al. [2006] note, bubble rise velocities are size dependent, but this dependency itself differs dramatically depending on whether bubbles are small enough to be considered as rigid spheres, or large enough to deform as they rise. For rigid spheres, the rise velocity, vsmall, is related to the equivalent diameter, de, via:

$$v_{\text{small}} = \left(\frac{4 d_e g (1 - \rho_g / \rho_w)}{3 C_D} \right)^{1/2}, \tag{10}$$

$$C_D = \frac{24}{\text{Re}} + \frac{3}{\sqrt{\text{Re}}} + 0.34, \tag{11}$$

$$\text{Re (Reynolds number)} = \frac{\rho_w v_{\text{small}} d_e}{\mu_w}, \tag{12}$$

where g is the gravitational constant, ρ_g and ρ_w are the densities of gas and water, respectively, C_D is the drag coefficient, and μ_w is the dynamic viscosity of water [McGinnis et al., 2006]. Equations (10)–(12) can be solved iteratively to obtain a curve for v_{small} versus d_e.

Larger bubbles that can deform follow a second relationship between velocity, v_{large}, and d_e [McGinnis et al., 2006]:

$$v_{\text{large}} = \left(\frac{2 \sigma_w}{d_e (\rho_w + \rho_g)} + \frac{g d_e}{2} \right)^{1/2}, \tag{13}$$

where σ_w is the water–gas interfacial tension. A study by Wüstneck et al. [2007] suggests a single value for surface tension, 0.0725 N/m, should be used for water in the presence of either air or xenon. McGinnis et al. [2006] use the method of Jamialahmadi et al. [1994] to combine Eqs. (10) and (13) and obtain a single relation between velocity and bubble size:

$$v_{\text{combined}} = \left(v_{\text{small}}^{-2} + v_{\text{large}}^{-2} \right)^{-1/2} \tag{14}$$

The parameters used to obtain curves for Eqs. (10)–(13) are given in Table 2 [Sifner and Klomfar, 1994].

Curves for the small, large and combined bubble rise velocities are shown in Fig. 13. In general, the predicted combined velocity curves indicate a transition from a steep dependence of velocity on bubble diameter for small bubbles to a slower velocity increase with bubble diameter for larger bubbles. Water density exerts a far more significant control on the curves than the relatively small gas densities, but the large molecular weight of xenon is enough to slightly lower the xenon curves

Table 2. Parameters used in Equations (10)–(13) to generate curves shown in Figure 13.

Parameter	Value
Density of air, ρ_{air}, 25 °C, 1 MPa [kg/m^3]	11.7
Density of water, ρ_{water}, 25 °C, 1 MPa [kg/m^3]	997
Density of water, ρ_{water}, 9.7 °C, 1 MPa [kg/m^3]	1000
Density of xenon, ρ_{xenon}, 25 °C, 1 MPa [kg/m^3]	55.3
Density of xenon, ρ_{xenon}, 9.7 °C, 1 MPa [kg/m^3]	59.4
Gravity, g [m/s^2]	9.8
Surface tension of water, σ_w [N/m]	.0725
Viscosity of water (dynamic), μ_w, 25 °C, 1 MPa [Pa·s (x10^{-6})]	889
Viscosity of water (dynamic), μ_w, 9.7 °C, 1 MPa [Pa·s (x10^{-6})]	1316

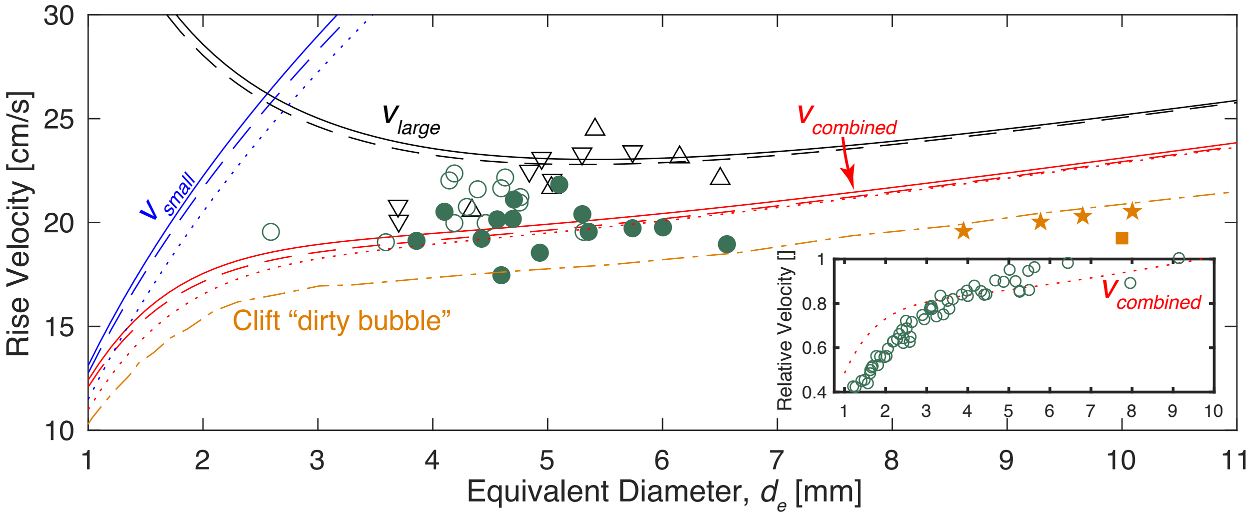

Figure 13. Rise velocity dependence on bubble size. Equations for small bubbles (Eq. (10), v_{small}, blue curves), large bubbles (Eq. (13), v_{large}, black curves), and their combination (Eq. (14), v_{combined}, red curves) are plotted using the parameters from Table 2. Solid curves are for air at 25°C and 1 MPa, and are essentially indistinguishable from the curves for air at 25°C and 0.7 MPa (not plotted for clarity). Dashed curves are for xenon at 25°C and 1 MPa, showing a small offset with the solid curves due to the increased density of xenon relative to air. Dotted curves for xenon at 9.7°C and 1 MPa are offset from the dashed lines primarily because the water viscosity change between 9.7 and 25°C (Eq. (10) and (14) only). Dot-dashed orange curve is digitized from Clift et al. [1978] for air in contaminated water. Open symbols are hydrate-free bubbles of air (black triangles: 1 MPa; inverted triangles: 0.7 MPa) and xenon (circles). Differences due to density are not observable. Solid symbols are for hydrate-coated bubbles of xenon (solid green circles) and of methane (orange stars: 6.9 MPa data from Maini and Bishnoi [1981], orange square: Warzinski et al. [2014]). Though the rise velocity dependence is weak for de >2.5 mm, data from captured, hydrate-free xenon bubbles (open circles, inset) verifies the stronger dependence for smaller bubbles suggested by the theoretical curves.

(dashed curves) relative to their values for air (solid curves). Water viscosity, which appears only in the small-bubble velocity calculation, has a large enough temperature dependence between 9.7

and 25°C to modify the transition between steeply and slowly increasing velocities with increasing equivalent bubble diameter (dotted curves). Fig. 13 also contains an additional curve for air bubbles rising in contaminated water, digitized from Figure 7.3 in Clift et al. [1978] (dot-dash curve), that has been used to describe the rise velocity of hydrate-coated "dirty bubbles" (e.g., [McGinnis et al., 2006; Wang and Socolofsky, 2015]).

Considering the hydrate-free bubbles of air and xenon (open symbols in Fig. 13), velocities plot primarily between v_{large} and v_{combined}, with air and xenon rise velocities overlapping in spite of their density differences. Overlap is expected given the small predicted velocity differences due to gas density differences (solid versus dashed curves). Xenon hydrate-coated bubbles (solid circles in Fig. 13) are slightly slower than hydrate-free bubbles, and are fairly well predicted by the v_{combined} curve.

Previous measurements of methane hydrate (solid orange symbols in Fig. 13) plot close to, but slightly below the "dirty bubble" curve from Clift et al. [1978]. To zeroth order, rise velocity data for bubbles with hydrate shells suggests there is very little dependence of rise velocity on bubble size, and that an approximate rise velocity estimate of 19–20 cm/s could be applied. This estimate is on the high end of the ∼15–20 cm/s range measured by Wang et al. [2016] on naturally-occurring methane hydrate-coated bubbles from seafloor seeps in the Gulf of Mexico. Wang et al. [2016] also showed rise velocities were essentially independent of bubble size (observed bubble sizes: $2.5 < d_e < 9$ mm).

As shown in Fig. 13, the transition to a stronger dependence of rise velocity on bubble diameter is predicted for bubble diameters below ∼2.5 mm. In bubble capture tests on hydrate-free xenon bubbles in which single bubbles were captured and observed over time as they dissolved and shrank, the transition between strong and weak dependence of rise velocity on bubble size was observed for de between 2 and 3 mm (Fig. 13, inset). This transition was also observed in the field, where Wang et al. [2016] found rise velocities dropped to ∼8–12 cm/s for bubbles with de near 1.5 mm.

One reason for the apparent independence of rise velocity on bubble size for hydrate-coated bubbles with de >2.5 mm is bubble shape. As shown by the open symbols in Fig. 14, hydrate-free bubbles can deform, leading to a balance between rise velocity, bubble size and bubble flatness. Larger bubbles rise faster, but an increased rise rate also flattens the bubble, limiting the velocity increase with size. This weak dependence of bubble velocity on bubble size due to flattening is captured in v_{large} (Eq. 13). In contrast, hydrate formed so quickly in the xenon hydrate rise rate experiments discussed here that bubble shapes were likely frozen into place as each bubble escaped the gas inlet orifice. As a result, hydrate-coated bubbles (solid circles in Fig. 14) took on random shapes which were maintained by the rigid hydrate shell during their observed rise. Bubbles that were relatively flat for their size suffered more from drag than bubbles that were relatively spherical for their size, and hence these relatively flat bubbles rose more slowly. Thus, the size and shape became independent controls on rise velocities for hydrate-coated bubbles, obscuring the weak dependence of rise velocity on bubble size observed for hydrate-free bubbles with dynamically-determined bubble shapes.

Bubble size and shape were nearly independent in the xenon hydrate tests described here because hydrate formation was rapid. In natural marine systems, relatively low dissolved methane concentrations in the water column result in bubbles being released from seafloor seeps and rising into the water column prior to forming hydrate, as observed by Wang et al. [2016]. These bubbles could potentially reach their terminal velocity and dynamically-determined shape prior to acquir-

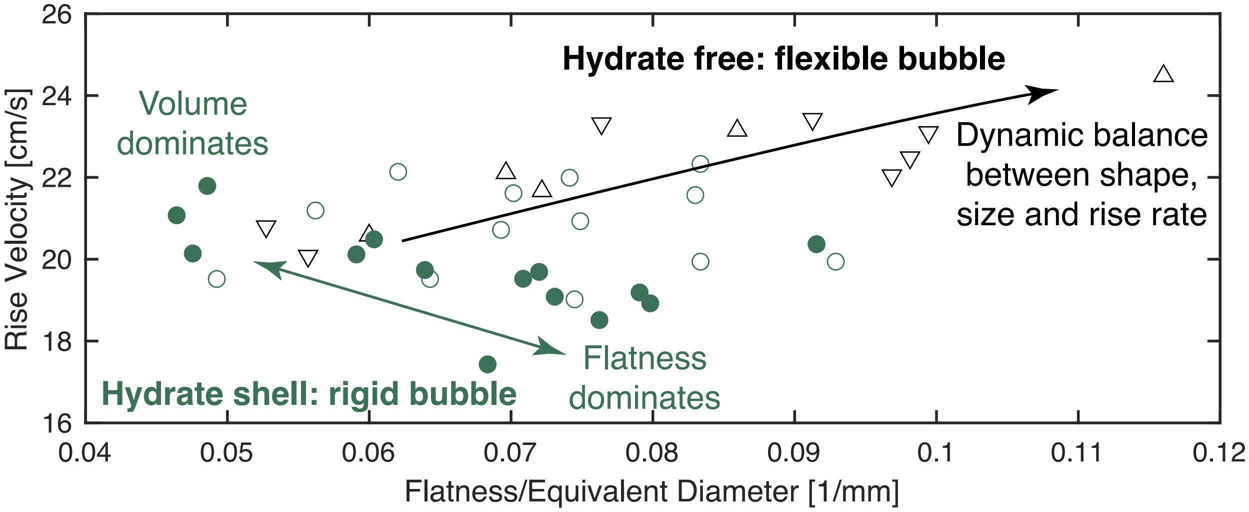

Figure 14. Dependence of rise velocity on shape. Symbol meanings are the same as in Fig. 13. Bubble flatness is scaled by the bubble's equivalent diameter to highlight shape-dependent, rather than size-dependent, differences between bubbles with flexible versus rigid surfaces. The dynamic relationship between size, rise rate and shape in hydrate-free bubbles (open symbols) is illustrated by a slight positive trend in rise rate as larger, faster-rising bubbles flattened relatively more than smaller, slower bubbles. Bubbles with hydrate shells (solid green circles) acquired fixed shapes as they were emitted from the gas inlet, so their flatness was not related to size. Consequently, bubbles that were flat relative to their size rose more slowly than bubbles that were spherical relative to their size, producing a slightly negative trend with rise rate.

ing a hydrate shell. Even so, Wang et al. [2016] observed hydrate-coated bubbles with a variety of fixed, non-ellipsoidal shapes, indicating that some bubbles had their shapes frozen into place by hydrate shell formation before those bubbles could be shaped in the same dynamic fashion as the hydrate-free bubbles modeled in Eq. (13) and (14). There are also indications of some seafloor seeps having local dissolved gas saturations high enough to cause hydrate formation on a bubble's surface as the bubble emerges from the seafloor [Expedition EX1402L3 Scientists, 2014]. Irregular bubble shapes, locked in by their rigid hydrate shells, likely contribute to the apparent lack of rise rate dependence on bubble size.

2.5 Conclusions

This study provides laboratory observations of rising bubbles with and without hydrate shells that can be used to gain insight into the evolution and rise rate of bubbles emitted from seafloor seeps. One primary control on the manner in which a gas such as methane dissolves out of a hydrate-coated bubble is the condition and behavior of the bubble's surface. Unless bubbles form hydrate shells extremely rapidly due to high dissolved-gas saturations and pressure-temperature conditions that are far into the hydrate stability region, bubbles will likely develop uniform shells and quickly transition away from a tendency to shed flakes of pure hydrate. As bubbles rise, their sizes evolve in response to competing drives toward shrinkage and expansion. Bubbles tend to shrink as gas dissolves out of the bubble and into the surrounding water, or shrink as gas is consumed to create or thicken a hydrate shell on the bubble's surface. The size of rising bubbles also responds to expansive processes, such as the addition of molecules of different gases to the bubble via stripping of dissolved gases from the water column, or expansion simply due to the decreasing pressure as the bubble rises. Hydrate-coated bubbles observed in this study were able to collapse and expand without seeming to rupture, though additional work on bubbles depressurized soon after formation is required.

A second primary control on the fate of a rising bubble is its rise velocity, which depends strongly on the condition of the bubble surface. A hydrate-free bubble has a flexible surface which is flattened by the drag of water as the bubble rises. The dynamic balance between bubble size (larger bubbles rise faster), bubble flatness (shape) and rise rate results in only a gentle velocity increase with increasing bubble size. By comparison, hydrate-coated bubble shapes are fixed and more randomly varied. This variability can obscure the small rise-velocity increase with increasing bubble size observed for hydrate-free bubbles. In practical terms, this shape variability effect for hydrate- coated bubbles means a nearly size-independent, constant velocity can be assumed for bubbles with effective diameters between $\sim$2.5 and 10 mm. A constant rise rate of 19–20 cm/s would be consistent with laboratory results. Field results [Wang et al., 2016] suggest a broader range of 15–20 cm/s is acceptable.

3 Field data analysis to link models and laboratory data to real world gas hydrate dynamics

3.1 Quantitative analysis of newly-discovered US Atlantic margin methane plumes

Acoustic backscatter data have been collected over newly-identified natural seeps on the western US Atlantic margin [Skarke et al., 2014]. These data were collected using both an 18 kHz Simrad EK60 split-beam echosounder (SBES) and a 30 kHz Kongsberg EM302 multibeam echo-sounder (MBES) on the Okeanos Explorer. The acoustic observations exploit the bubbles mechanical resonance and large acoustic impedance constrast with the surrounding water, and are similar to those made by other investigators [Merewether et al., 1985; Dimitrov and Dontcheva, 1994; Hornafius et al., 1999; McDonald et al., 2002; Heeschen et al., 2003; Greinert et al., 2006; Kannberg et al., 2013; Weber et al., 2014; Jerram et al., 2015]. The objective here was to examine the information contained within the acoustic backscatter records (the observed height of the anomalies associated with rising gas bubbles, the depth-dependent acoustic target strength) and to compare that information from that which would be predicted by models of gas bubble evolution [McGinnis et al., 2006; Gros et al., 2016, 2017], to examine the question of whether the models and observations are consistent.

3.1.1 Acoustic data analysis

The acoustic data used in this work are drawn from the gas-bubble seeps observed in 2012 and 2013 on the *Okeanos Explorer* [Skarke et al., 2014]. These seeps are distributed in water depths ranging from 300 m to 2200 m, extending along the western Atlantic Margin (Figure 15). The acoustic observations made by both the SBES and MBES exploit the strong acoustic scattering properties of gas bubbles in the ocean. Put simply, the gas bubbles act as mechanical resonators, with the gas inside of the bubble acting as a compressible spring and the entrained ocean water surrounding the bubble acting as a mass. When excited by an acoustic wave near the bubble's resonance frequency, the scattered acoustic field can be sufficiently strong to see individual bubbles at ranges exceeding 1000 m. Above resonance, the scattered acoustic field is related to its geometric cross section, and below resonance the bubble is within the Rayleigh scattering regime (see Clay and Medwin [1977] for a full description).

Example MBES data from a single ping (i.e., a single sonar transmission) is shown in Figure 16. Gas bubble plumes are visible as regions of high backscatter, with very high aspect ratio (height to width). Seep observations in these data are confounded by volume reverberation from marine organisms, which often present as horizontal bands (low aspect ratio), and reverberation from the seabed which presents in the data as noise 'rings' at constant range, coincident with the range to the seabed. The seep observations are also transient, appearing in only 1-2 pings at any one depth, although they can sometimes appear through several subsequent pings depending on how local currents are horizontally advecting the bubbles as they rise.

Automated processing routines were used to extract information from the MBES regarding the gas bubble plumes, including the rise height (maximum vertical extent of the acoustically observable plume) and the apparent seep target strength (TS). It should be noted that the MBES

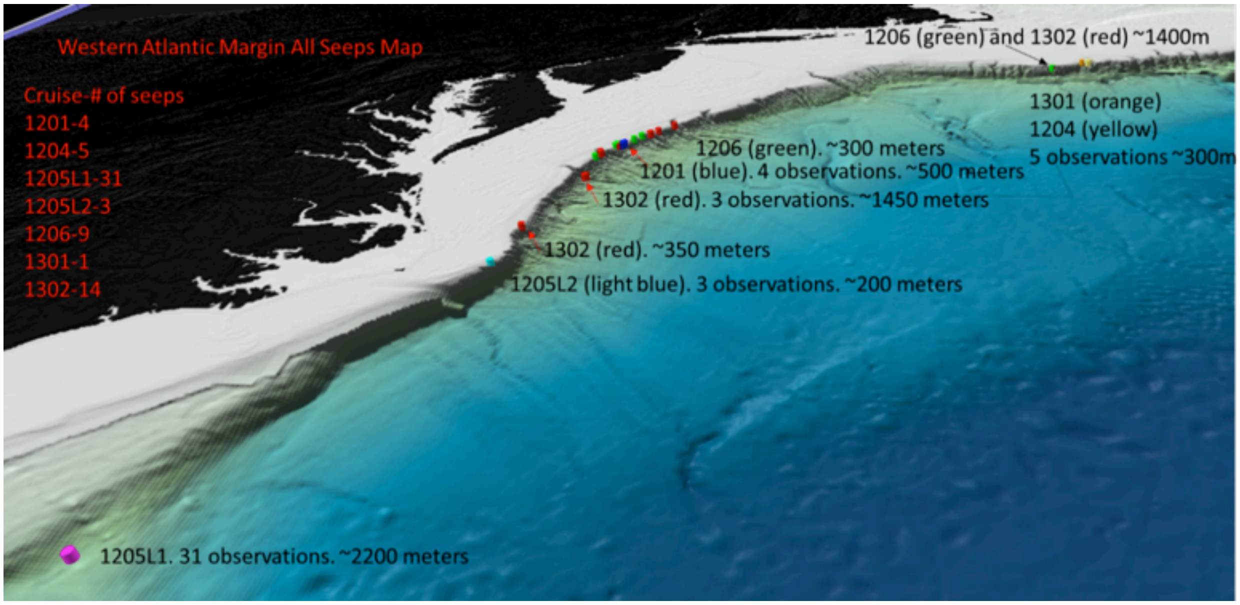

Figure 15. Map of SBES gas plumes on the US Atlantic margin, and that were examined as part of the present work.

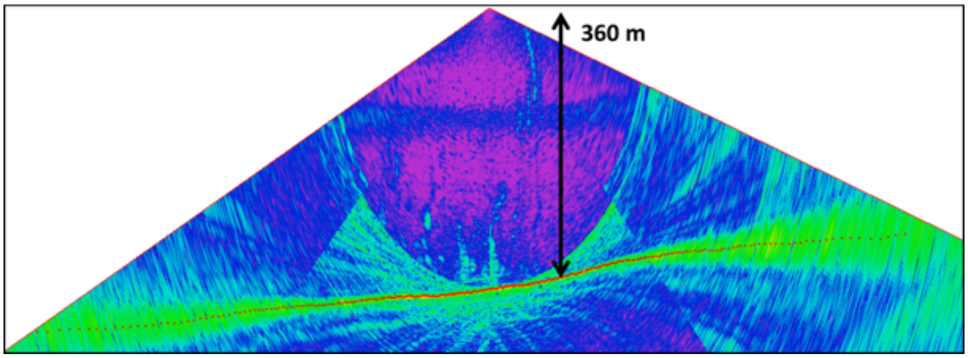

Figure 16. A single ping from the 30 kHz MBES, showing several vertical gas-bubble plumes including approaching the surface. The seabed is depicted as a series of red dots. Hotter (i.e., red/green) indicates stronger acoustic scattering.

data, unlike the SBES data are not calibrated, and so the seep TS derived from the MBES can only be used to infer general behaviors (e.g., observations of bubble resonance). The processing routine exploits the transient nature of the observations, and constructs a constant-false-alarm rate (CFAR) detector [Weiss, 1982] [Weiss, 1982] based on a local running mean of the observations based on a time history of several 10's of pings. This local mean, a function of beam angle and range, is then subtracted from an individual ping in order to generate an estimate of the signal-to-noise ratio (SNR) for transient (i.e. appearing in only 1-2 pings) targets. The resulting targets are then clustered (spatially co-registered), clusters with only a few targets are classified as noise and rejected, and the resulting targets are then geo-referenced and manually scrutinized in order to reject anomalies (typically coherent noise that manifests as unnatural vertical lines, or sidelobe interference that manifests as arcs of targets at constant range). Example results from this process are shown in Figure 17.

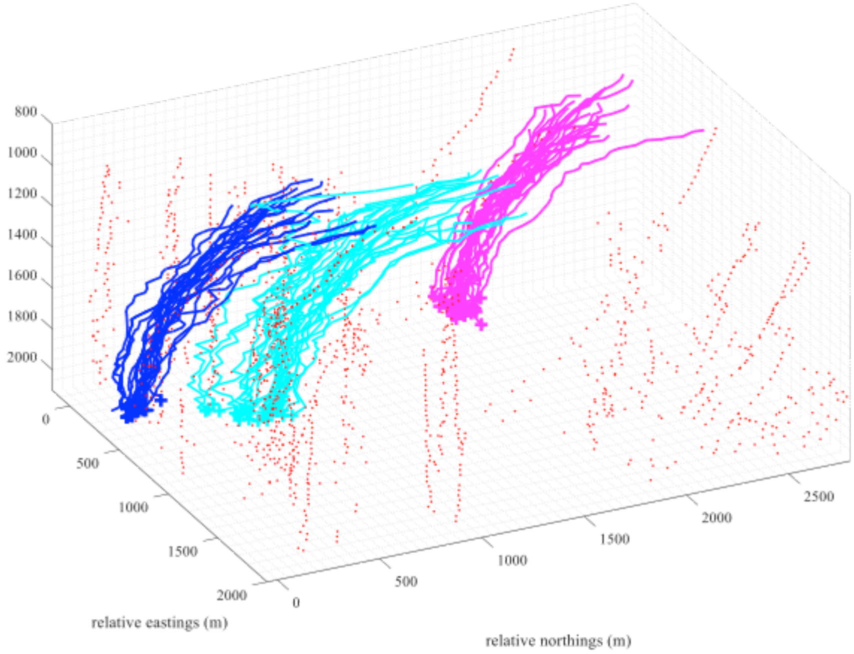

Figure 17. Multibeam echo sounder observations (dark blue, cyan, magenta) of gas seeps 'bending' in the current at Blake Ridge, rising from 2200 m to nearly 800 m water depth. False targets have been manually scrutinized and rejected (red dots). Note that multiple passes are overlaid on this plot.

Gas bubbles seeps manifest similarly in the SBES data, appearing as high-aspect ratio regions of high backscatter (Figure 18). In contrast to the MBES, the SBES data used in this work have a beam resolution that is an order of magnitude larger, causing the seeps to appear far wider than they actually are. The SBES employs a split-aperture, which can be used to position targets within the beam [Burdic, 1991] in order to make a beam-pattern correction for the estimated seep TS, as well as to calibrate the SBES using standard target techniques [Demer et al., 2015]. Seep TS estimates are extracted from the SBES data using techniques similar to those used for the SBES. The advantage of the SBES results, however, is that the data are calibrated and can be quantitatively compared to models of gas bubble TS. Further, the split-beam positioning can identify/detect whether the gas bubbles disappear from 'acoustic-view' because they became weak scatterers (due to dissolution, presumably), or because they were advected out of the beam by local currents [Jerram et al., 2015].

One of the difficulties in processing the SBES data is that the TS is often masked by the background noise, either because the gas-bubble targets are weak or because the background noise is high (Figure 19). To mitigate this issue, a process was developed to deconvolve the seep TS from the background noise [Pillsbury, 2015]. This process assumes the background noise is Rayleigh-distributed, and uses regions adjacent to the plume to estimate the depth-dependent Rayleigh parameter. A global search is then conducted for the Rayleigh parameter of the gas-bubble targets in order to find the best-fit between the observation and the sum of the two Rayleigh distributions, resulting in a refined estimate for the gas-bubble TS estimate independent of the additive background noise.

The MBES and SBES analyses were focused on gas seeps observed at Blake Ridge (Figure 20).

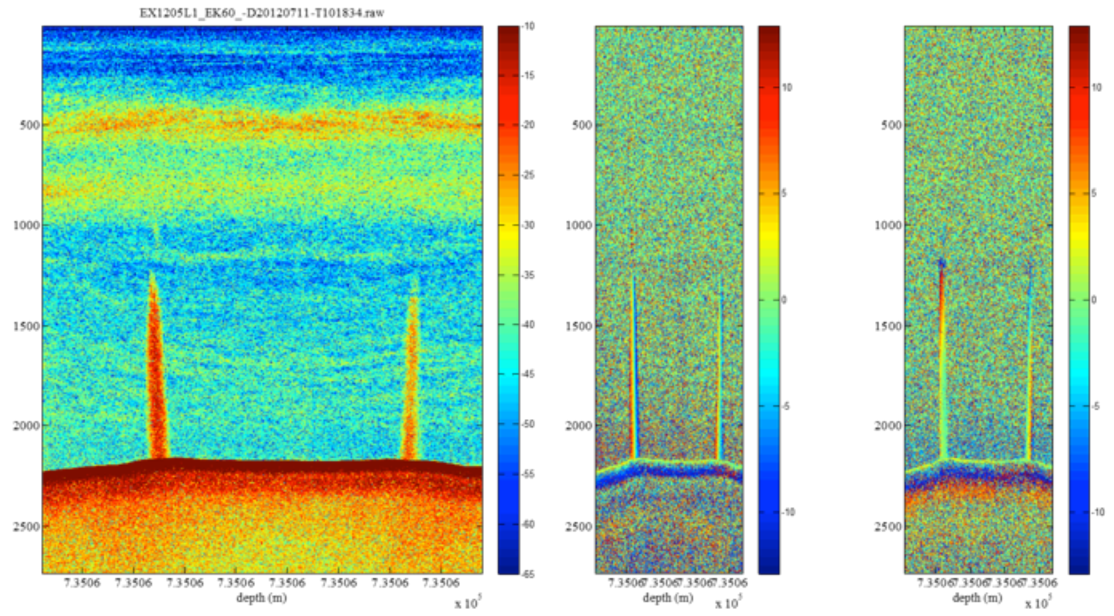

Figure 18. SBES observations of gas-bubble seeps rising from Blake Ridge. Left: SBES backscatter, showing two separate observations of gas seeps. Middle and right: split-aperture correlation positioning of the gas bubbles in the along-track and across-track directions, used to position the seep observations within the beam.

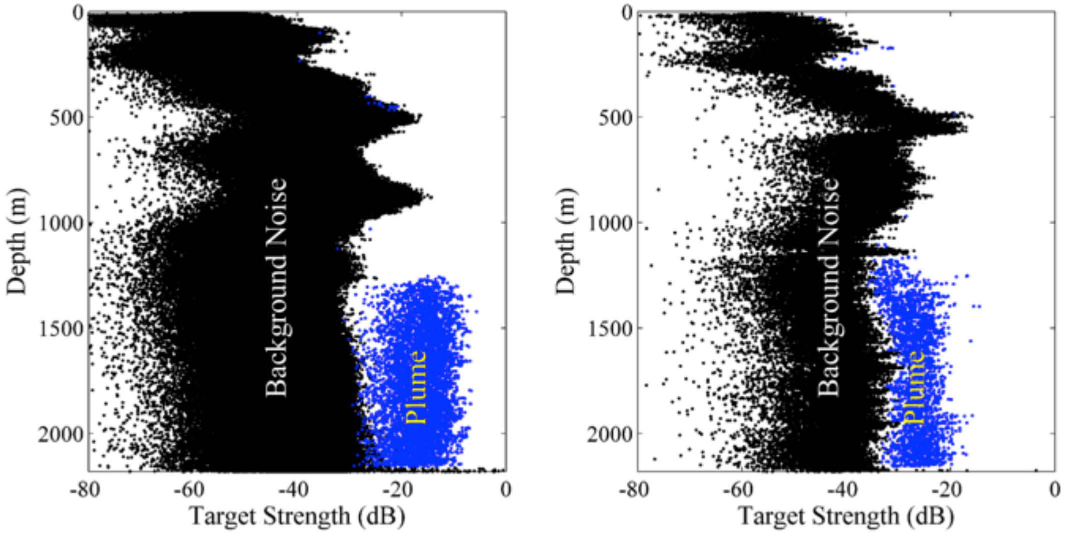

Figure 19. Example data from methane gas seeps observed in on the US Atlantic margin. The gas-bubble targets observed on the left are sufficiently strong that they can be rather simply separated from the background noise profile using a noise-thresholding approach. The gas-bubble targets on the right, however, have target strengths that overlap considerably with the background noise, and the estimate seep TS shows the imprint of the depth-dependent noise profile.

This well-known area [e.g., Holbrook et al., 1996; Dover et al., 2003] has several advantages including being data rich with more than 30 transects at close (∼40 m) line spacing, well known gas composition (100% methane), and depths (∼2200 m) that largely constrain the gas-bubble plume observations within the bathypelagic zone where volume reverberation from marine organisms is low. In this region, three persistent seep sites (referred to in Figure 20 as site A, B, and C) appear in the data. MBES data show for more than 30 transects, conducted over several days, show that the maximum height of the acoustically observable plume at 30 kHz reaches 800-900 m, well within the gas hydrate stability zone. TS profiles for the 18 kHz SBES data (Figure 21) show a consistent weakening of acoustic backscatter at depths shallower than 1200 m, with acoustic observations decaying into the background noise at 1000 m, coinciding with the base of the deep scattering layer (DSL). There are no obvious resonance peaks in the plume, for either the MBES or SBES data, making it likely that the gas bubbles have a wide range of sizes.

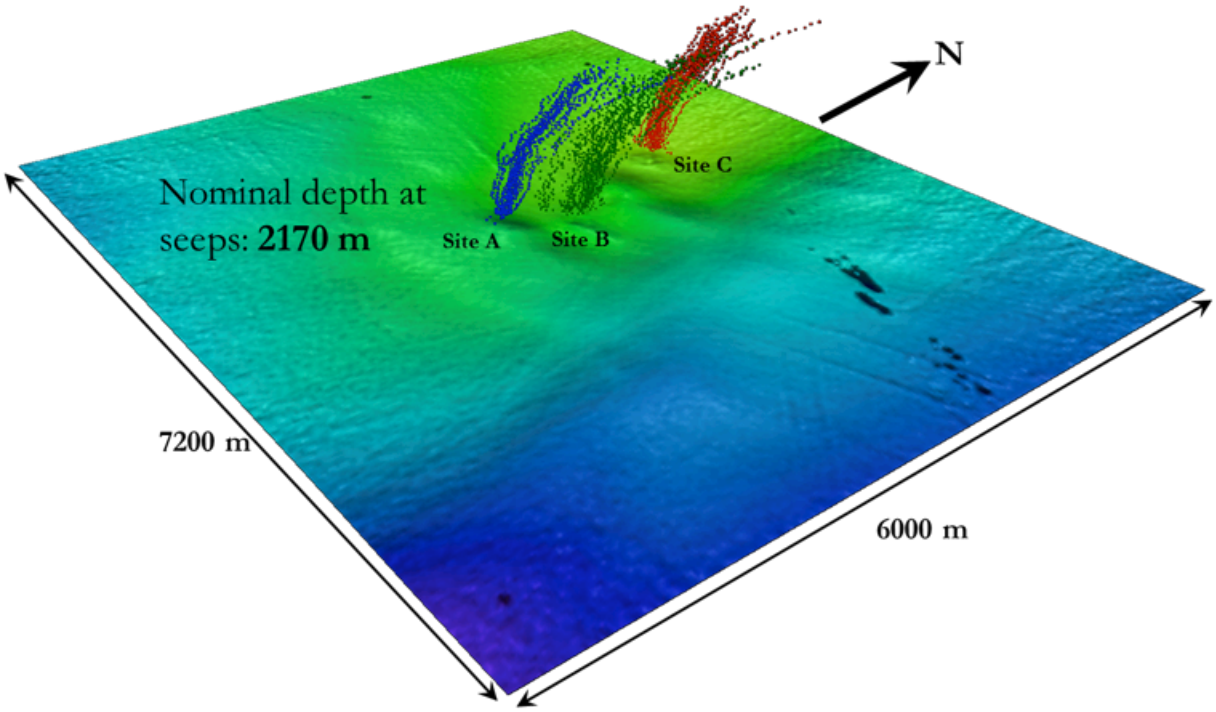

Figure 20. Seeps observed with the MBES (through multiple passes) at Blake Ridge.

3.1.2 Gas bubble modeling and comparison with data

Two different types of models were explored to aid in the interpretation of the acoustic data: a bubble 'evolution' model, describing the size and gas composition of the bubble as it rises through the water column, and acoustic scattering model describing the frequency-dependent acoustic response of the bubble. The TAMOC model [Socolofsky et al., 2015] was used to describe the bubble evolution. This model was seeded with 100% methane bubbles at a depth of 2170 m, and with bubble diameters ranging from 1-12 mm. The results show profiles of the size and mass concentrations for CH4, O2, N2, and Ar (Figure 22). The bubbles undergo a size-dependent hydrate-rind formation time, after which the bubble dissolution slows dramatically. During the bubble ascent, the original

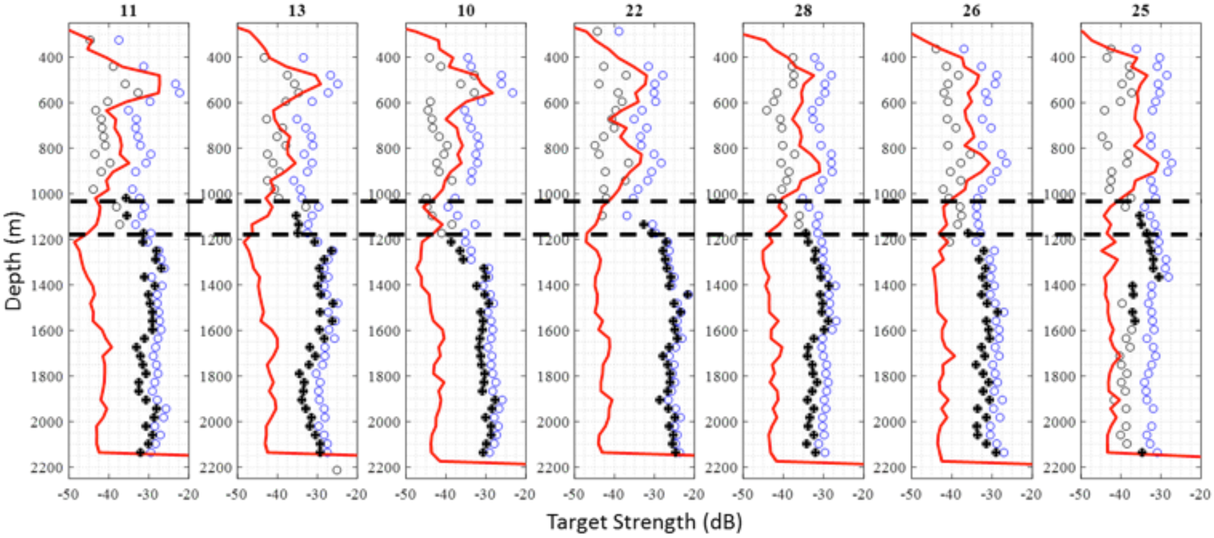

Figure 21. SBES observations for 7 passes over the gas-bubble plumes at Blake ridge. Each subplot shows the background noise (red line), the initial observation of plume target strength with potential corruption by background noise, and the deconvolved (true) gas-bubble plume TS. The selection criteria for these observations was that the acoustically-observable top of the plume was well within the beam footprint.

CH4 is transferred into aqueous concentration, and O2, N2, and Ar are transferred from aqueous concentration into the bubble. Depending on the size of the bubble and the aqueous concentration of gases, the O2, N2, and Ar that has entered the bubble eventually returns to aqueous concentration. Bubbles escaping the seabed at sizes smaller than ∼3 mm radius (6 mm diameter) do not survive to depths shallower than 1400 m, and so would not contribute to the shallower portions of the acoustically-observed seeps described in the previous section. Similarly, gas bubbles greater than ∼6 mm radius (12 mm diameter) survive to the sea surface, although almost all CH4 has been lost to aqueous concentration during the ascent. According to this model, the top of the gas-bubble plume appears to be constrained to gas bubbles which are between 3-6 mm in radius.

The acoustic scattering from the gas bubbles can be modeled as either fluid spheres (e.g., pure gas), fluid shells surrounding a fluid sphere, or as elastic spherical shells Goodman and Stern [1962]; Stanton [1990]; Jech et al. [2015]. In the latter two cases, the effect of hydrate coatings on the bubble are considered using properties (compressional wave speed: 3650 m/s, shear wave speed: 1890 m/s, density: 900 kg/m3) previously measured by Waite et al. [2000]. Acoustically, the presence of the shell acts to increase the resonance frequency compared to that of the fluid sphere model, and to alter the higher-order mode in the scattered response (Figure 23). One of the difficulties in this modeling is knowing the shell thickness: thin hydrate shells exhibit little change from the hydrate-free model, while thick shells show a relatively large change in behavior. Previous laboratory observations [Li et al., 2013] suggest that the hydrate thickness may likely be as thin as 100 μm, although after long durations the shell exhibits greater thickness, buckling, cracking, etc., which is not included in the models described here.

Both the bubble evolution and acoustic scattering models were combined to provide profiles of predicted acoustic TS for comparison with the observations (Figure 24). These comparisons are shown for both 18 kHz and 30 kHz, corresponding to the SBES and MBES observations,

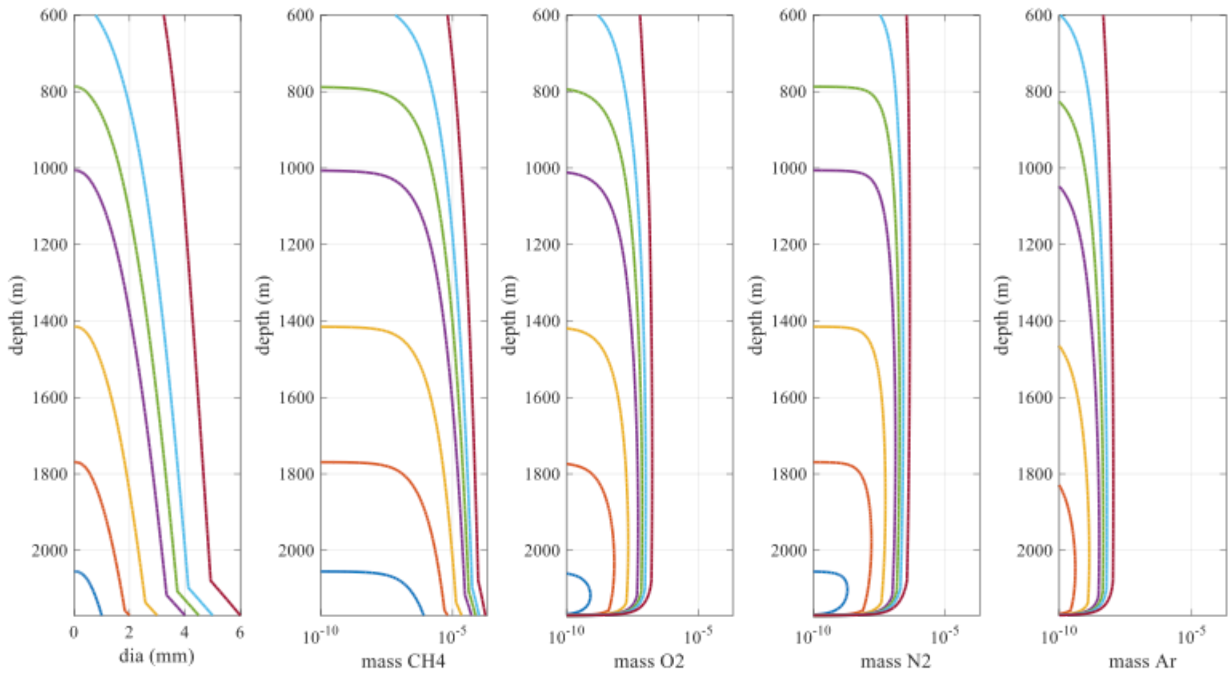

Figure 22. Results from the TAMOC model [Socolofsky et al., 2015] for 1-6 mm diameter bubbles seeded at a starting depth of 2170 m.

respectively. The presence of the hydrate shell is present, but does not drastically change the modeled acoustic response: based on these models, the presence of the hydrate shell would result in a bias in the estimated size of the bubble contributing to the acoustic response but would not alter the general trend.

According to the 18 kHz modeled results, a 4.5 mm radius bubble leaving the seabed would enter the Rayleigh-scattering regime, and thus be largely unobservable, at depths shallower than 1100 m, and subsequently become completely dissolved at ∼800 m water depth. The same bubble would be observable to ∼850 m at 30 kHz. This is consistent with the minimum observed depths of the plume in the acoustic data, and no evidence for larger bubbles is present within the data. The calibrated 18 kHz observation show TS values that are 5-8 dB higher than the model for single bubbles, which suggests that there are 3-5 bubbles of this size contributing to the acoustic response at water depths between 1100-1200 m. Resonance peaks shown in the single-bubble models but not present in the observed acoustic response suggest that there is a wide distribution of bubble sizes contributing to the response, with smaller bubbles being ‘stripped out’ of the water column as they rise due to dissolution. At 18 kHz in this depth of water, the acoustic response is sensitive only to bubbles greater than 3.5 mm radius; at 30 kHz, the acoustic response is sensitive to 2+ mm radius bubbles.

3.1.3 Conclusions from acoustic data analysis

The analysis of SBES and MBES data collected on the western Atlantic margin were focused on data recorded in deep water (∼2170 m) at Blake Ridge. These data offered the best opportunity

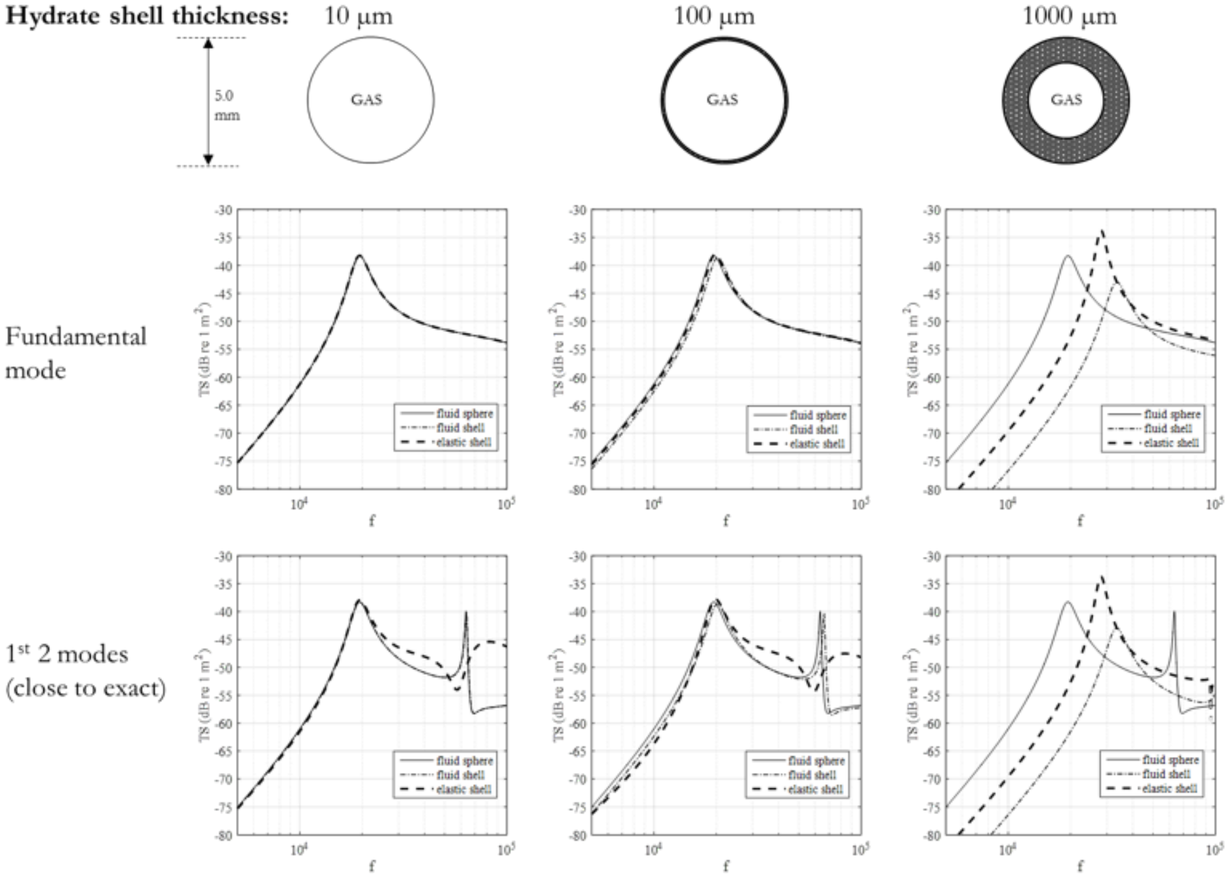

Figure 23. Scattering models for CH4 bubbles for fluid sphere, fluid shell, and elastic shell models for three different shell thicknesses. The top row of models incorporates only the fundamental scattering mode, and the second row incorporates the 1st and 2nd modes.

for comparing data and existing models: the deep water depths mitigated masking of the acoustic observations by the shallower DSL, and maintained the bubbles within the gas hydrate stability zone for some 1500 m during their ascent (if they survived that long). The Blake Ridge data set was also very comprehensive, with 30+ lines of data at 40 m line spacing, providing high confidence that the top of the plumes were observed. Processing techniques were refined, in the case of the MBES, or created, in the case of the SBES noise deconvolution, as part of this work, to analyze these data, and these techniques are now available for future studies.

The primary objective of these work was to establish whether the observations from the Atlantic margin were consistent with existing models. Both model and observation were found to provide a plausible match, assuming that a 4.5 mm radius bubble is a reasonable upper limit for bubble size distributions, that the hydrate coating on the shell was on the order of a 100 μm (that is, it did not dominate the mass distribution in the bubble). This upper limit on bubble size is consistent with that observed by previous in-situ observations at other sites [e.g., Leifer and MacDonald, 2003; Sauter et al., 2006; Römer et al., 2012; Weber et al., 2014; Wang et al., 2016]. Further, the model-data comparison suggests that the acoustic observations are sensitive to the upper end (i.e., large size) of the bubble size distribution. No obvious resonance peaks were present in the acoustic data, suggesting that smaller bubbles are present as well, as is typically the case for natural seeps.

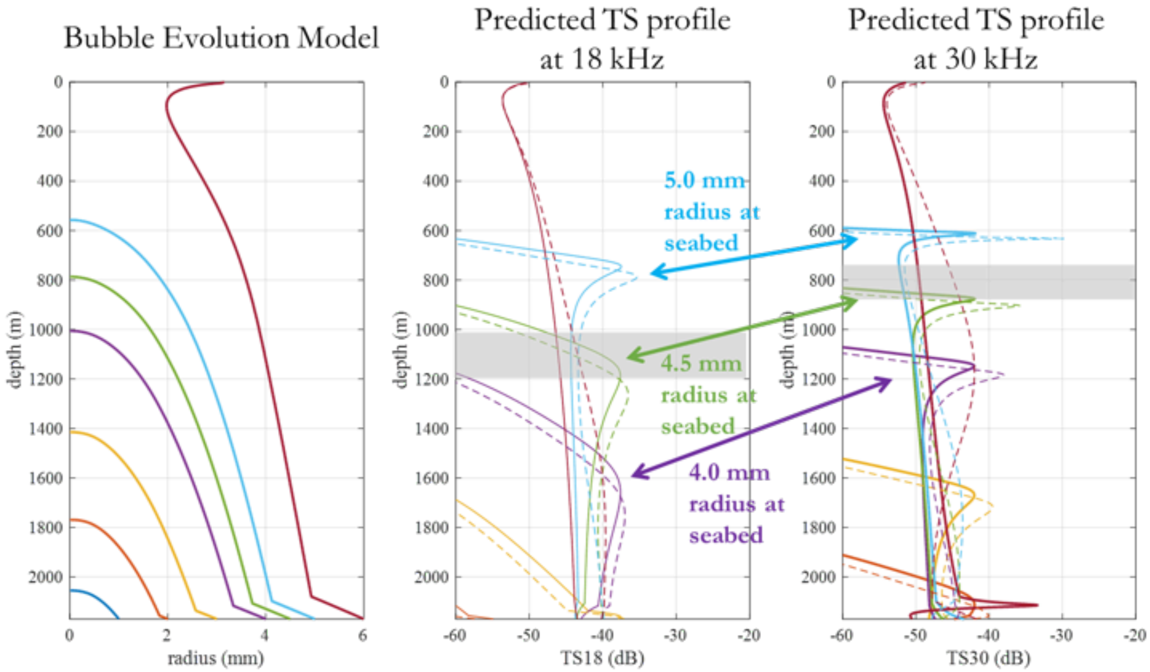

Figure 24. The combined acoustic and bubble evolution model showing the size of individual rising bubbles (left), and the predicted acoustic response for 'clean' and hydrate-coated bubbles at 18 kHz (middle) and 30 kHz (right).

Although not conclusive without absolute knowledge of the bubble size distribution, the model and data presented here are self-consistent.

3.2 Place US Atlantic margin seeps in regional and global context of gas hydrate system dynamics

The goal of this portion of the project was to build on the then-unpublished discovery of hundreds of methane seeps on the northern U.S. Atlantic margin (USAM) [Skarke et al., 2014] to consider conditions for gas hydrate formation in the water column on a global basis, to compile information about seep distributions on US margins (insofar as possible) and to use empirical information to determine the updip limit of gas hydrate stability on US margins. Although not funded by this project, Ruppel participated in [Weinstein et al., 2016] and led [e.g., Ruppel et al., 2015, 2018] a number of additional cruises on the northern USAM during the award period and is currently compiling an update to the Skarke et al. [2014] *Nature Geoscience* database to document the dozens of seeps discovered with USGS instrumentation over the past 4 years.

The theoretical and laboratory-based components of this project focused on the thermodynamics of hydrate shells forming on ascending methane bubbles [Fu, X. et al., 2018] and the properties of hydrate-armored methane bubbles [Waite et al., 2017]. In the real world, an important question is where ambient conditions are appropriate for the formation of hydrate shells on methane bubbles escaping from the seafloor. As part of this project, we used a world ocean temperature database to create a map of the expected top of gas hydrate stability (for pure methane) in the water column in the world?s oceans. Such a map not only brackets where gas hydrate bubble armors might enter a pressure-temperature zone not conducive to the survival of a hydrate shell, but also gives a rough approximation for the bathymetric depth at which the most landward occurrences of gas hydrate could be encountered in marine sediments. That empirical depth limit is better predicted using bottom water temperature data (see below) since the water column temperatures (a) are only gridded averages; (b) do not account for the impact of the bathymetry or the near-seafloor thermal boundary layer on deep ocean temperatures.

The map resulting from this calculation (Figure 25) shows that the North Atlantic has the most variation in depth to the top of gas hydrate stability in the water column, a result that partially reflects the strong influence of the Gulf Stream, particularly on the western (U.S.) side of the basin. The variation in the North Atlantic may also reflect the data though: Much denser temperature data are available to compute the average gridded temperatures in this area than in other basins. Only along the upper continental slope on the northern part of the USAM is the top of hydrate stability less than 600 mbsl. Globally, the most extreme depths for the top of gas hydrate stability are in the Arabian Sea and in the area affected by the southwardly flowing Agulhas Current, east of South Africa. Much of the North Pacific, including the area offshore the Western continental U.S. has surprisingly shallow depths (450-550 mbsl) for the top of gas hydrate stability in the water column. The coldest water columns are offshore the western part of the Alaskan North Slope in the Beaufort Sea and offshore Antarctica. In both places, the top of gas hydrate stability can be between 200-250 mbsl on average. It is important to note that this map does represent annual average temperatures. Earlier work at the USGS has shown that near-bottom temperatures on the Beaufort margin fluctuate so much during the shoulder season (August to October) that the top of gas hydrate stability in the sediments would have to migrate over a kilometer along the slope to remain in equilibrium with the bottom water temperature variations.

Another part of this task was compiling the loci of methane inputs into the ocean from seafloor seeps (example in Figure 26), with particular attention to US margins mapped using increasingly common water column imaging technologies. Research in the community has moved quickly in parallel with the duration of this project: Not long after this project was initiated, the NOAA Pacific Marine Environmental Laboratory (PMEL) and researchers at the University of Washington [Johnson et al., 2015; Merle, S. and Embley, R., 2016; Embley, 2017] began highlighting the discovery of seeps on the Northwest Pacific US margin, many found as a result of routine data collection by the D/V Nautilus. The number of seeps described by PMEL now numbers many hundreds, and Ruppel leads an investigator group that has obtained shiptime on the *R/V Falkor* to investigate aspects of seep dynamics on the upper continental slope in this area in summer 2019. Tom Weber had already been a part of quantitative work on seeps in the Northern Gulf of Mexico when this project started, and the NOAA ship *Okeanos Explorer* has over the intervening few years collected large amounts of water column imaging data that are publicly available for delineating seeps in this area. Other researchers in the community are now culling through vast quantities of data to map out the seep distributions in the northern Gulf of Mexico at the same time that some private sector firms have taken a multidisciplinary approach to systematically acquiring thousands of kilometers of data that fully covers the seafloor in the northern Gulf of Mexico and identifies natural “leak points” in the overall petroleum system. The seeps shown in Figure 26 for the northern Gulf of Mexico are not documented in one location, rather being spread among numerous publications focused on specific seeps. On the northern USAM, the USGS has taken part in or led six cruises since 2013 and substantially expanded the number of known seeps beyond

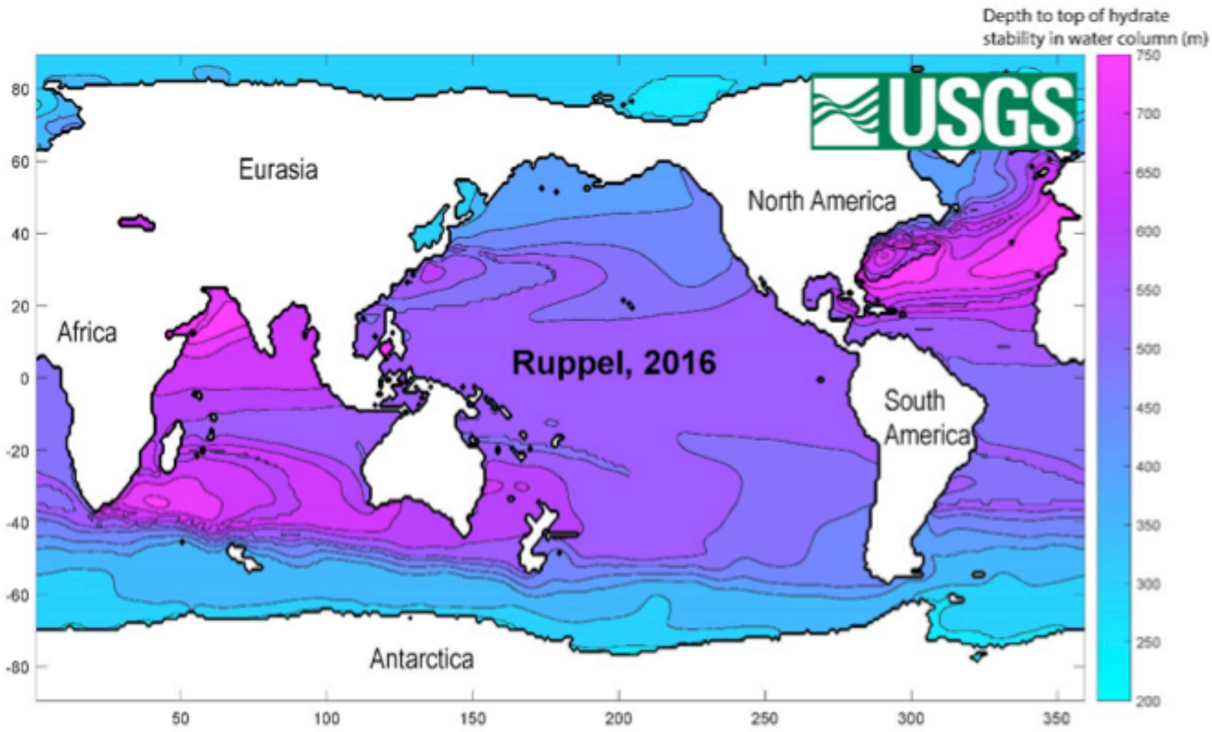

Figure 25. Depth to the top of the gas hydrate stability zone in the water column for pure methane hydrate, based on averaged annual temperatures as a function of depth in one degree blocks as provided in world databases.

those in the originally published Skarke et al. [2014] database. In the coming months, NOAA's Okeanos Explorer will acquire substantial amounts of new water column data for unexplored parts of the USAM, further enhancing the knowledge of seep distribution on this margin. On the U.S. Arctic margin, seep locations on the shelf have been identified by other government agencies and are not shown here. The USGS did attempt to analyze multibeam water column backscatter data acquired by the USCG Healy to look for seeps on the Arctic margin, but the data were found to not be of sufficient quality to support the analysis. The USGS has also compiled some seeps in non-US locations from the published literature and other sources during the course of this project.

It is important to note that seeps occur at many locations and for a range of reasons, mostly not related to gas hydrates. During the course of this project it came to be widely accepted in the hydrates community that most methane seeps deeper than ∼100 m water depth probably do not contribute methane directly to the atmosphere [Ruppel and Kessler, 2017]. Thus, mapping the non-hydrate related seeps in shallow water (shelf, delta, or estuarine) locations may have the highest priority for determining the contribution of marine seeps to the methane in the atmosphere. Only a small fraction of global seeps is likely to be directly linked to the degradation of gas hydrate on upper continental slopes. Furthermore, it is difficult to prove a direct linkage between leaking methane gas and underlying methane hydrate unless the hydrate contains a relatively unique mixture of gases that is also emitted at seafloor seeps known to be rooted in the hydrate stability zone.

There are numerous examples of seeps not originating with gas hydrate processes. For example, in petroleum basins like the Gulf of Mexico, seeps are often the direct effect of deep-seated salt migration, and the faulting that accommodates the salt and the heating of sediments due to the thermal properties of the salt combine to mobilize hydrocarbons and other fluids and create seafloor seeps. On the USAM, large numbers of seeps may originate due to erosional processes and canyonization [Skarke et al., 2014], processes that cut into the gas-charged upper continental slope and outer continental shelf, exposing gassy strata to seawater. On active margins offshore New Zealand and the Northwest U.S., faulting plays a predominant role in providing a pathway for fluids, including methane, to reach the seafloor at seeps, and no gas hydrate degradation may not be necessary to feed these seeps. In regional and global compilations, a certain set of deepwater seeps that occur at seafloor depths well within the gas hydrate stability zone continues to be considered anomalous, particularly in non-petroleum areas and at locations lacking salt diapirs [Skarke et al., 2014]. These deepwater seeps leak methane into the overlying ocean when the methane should be forming gas hydrate. Several physical reasons might explain the presence of free gas leaking at such profound water depths, and these seeps have added importance in this project because the methane emerges at depths where gas hydrate films are expected to form on the rising methane bubbles.

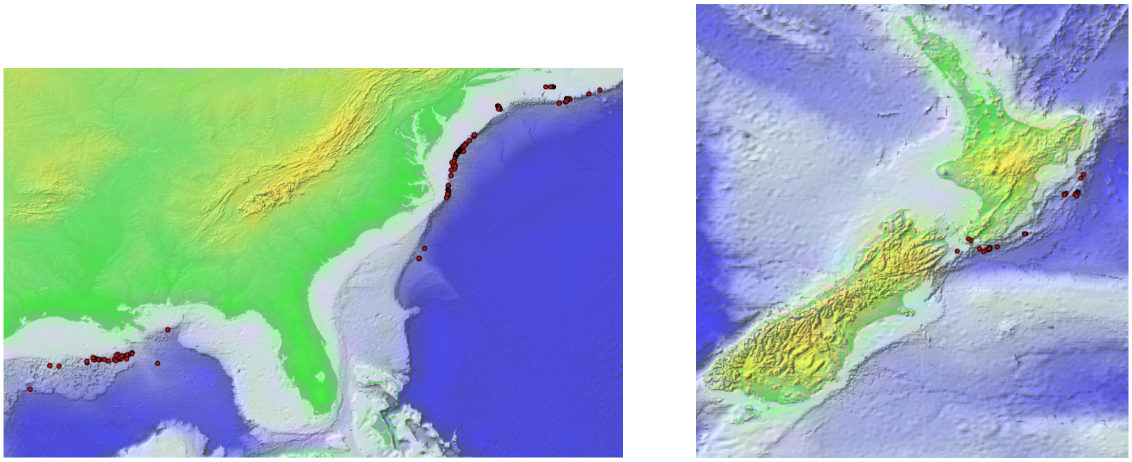

Figure 26. Examples of published and unpublished seep locations compiled for USAM/northern Gulf of Mexico (Skarke et al. [2014] and other NOAA data) and New Zealand margin [Greinert et al., 2010a]. Other compilations cover the remaining US margins and other global locations.

As noted above, the predicted top of gas hydrate in the water column can differ from the empirical landward limit of gas hydrate determined based on analysis of bottom water temperature data. In the course of this project, we wrote a Python code to analyze conductivity-temperature-depth (CTD) casts in the World Ocean Database and extract near-bottom temperatures from casts whose deepest reading was within 10% of the full-ocean depth at that location according to a bathymetric database. The rationale was that readings within 10% of the full-ocean depth at a site probably were within the nearly isothermal near-seafloor thermal boundary layer typically observed at water depths greater than the uppermost continental slopes. The resulting data were then compared to the gas hydrate stability curve calculated for pure methane hydrate and nominal saltwater salinity. A binary value was assigned to each point to indicate whether the bottom water temperature was within or outside the gas hydrate stability zone. The map was then manually contoured within ArcGIS to locate the landward limit of the gas hydrate stability zone.

An example result from this calculation is shown in Figure 27 for the U.S. Pacific Coast, with the white curve separating locations where gas hydrate is not stable (to the east) from those where it is (to the west). Nearly all the seeps delineated on the California margin by Lorenson et al. [2016] occur landward of the gas hydrate limit, and indeed most of these seeps are clearly identified as being related to hydrocarbon migration, not the presence of gas hydrates. Some newer seeps reported by the news media off Southern California are not represented in this map. Along the Oregon-Washington active margin, many of the seeps appear at the scale of Figure 27 to lie directly at the updip limit of empirically-determined gas hydrate stability. When viewed at a larger scale, the seeps are 7-10 km west of the hydrate limit off northern California and southern Oregon but much closer to the limit in the section landward of Hydrate Ridge. Notably, seeps on the U.S. Pacific Northwest margin as described by Merle, S. and Embley, R. [2016] generally lie seaward (deeper water) of the empirical updip limit. In contrast, most seeps delineated by Skarke et al. [2014] on the USAM lie landward (shallower depth) of the empirical updip limit. If a significant portion of these seep populations on both margins is related to gas hydrate processes, then this difference may underscore the role that local geologic features and oceanographic conditions play in determining the locations of the seeps relative to the landward limit of gas hydrate stability.

As a final component of this part of the project and other, related DOE-funded projects being conducted by the USGS, the USGS has been refining seep maps for the USAM. Figure 28 shows one example of this refinement, comparing the seeps identified in the Skarke et al. [2014] database and those identified in subsequent cruises for the area near Cape Hatteras, North Carolina. While this is a shallow-water area at the shelf-break in an area expected to have large numbers of seeps, refinements at other locations along the margin have revealed the presence of previously-unknown deepwater seeps [Ruppel et al., 2018] and also shown that upper slope seeps previously identified by Skarke et al. [2014] sometimes could not be found during subsequent surveys. The advent of new technology has clearly produced a revolution in the ability of marine scientists to identify marine methane seeps, and the next challenge will be determining which seeps contribute the most methane input to the ocean and how and whether those seeps are truly linked to the dynamics of the underlying gas hydrate system on upper continental slopes.

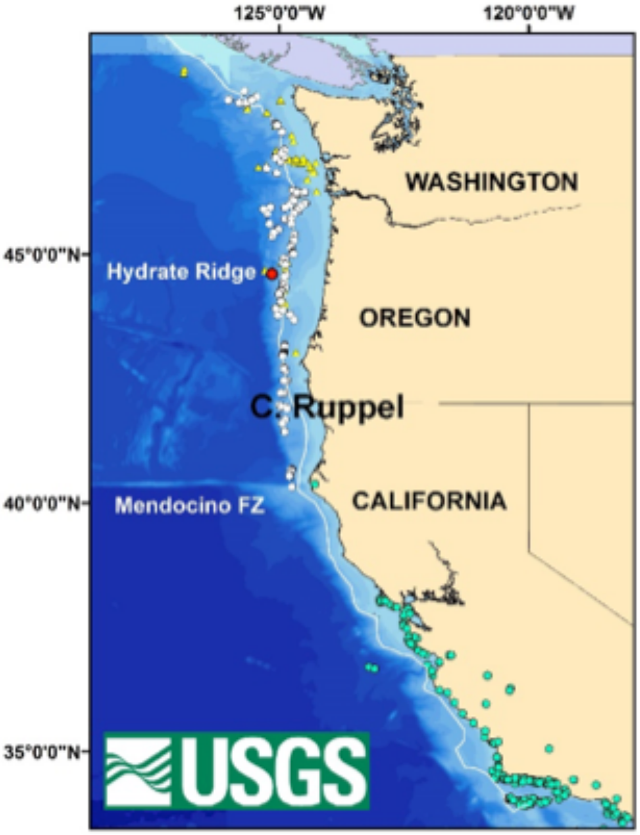

Figure 27. Compilation of published seep locations from Merle, S. and Embley, R. [2016] and Johnson et al. [2015] for the northern part of the US Pacific margin (white and yellow symbols) and from Lorenson et al. [2016] for the California margin south of San Francisco Bay (green circles). Hydrate Ridge is shown as the red dot. The white line is the empirically determined updip limit of gas hydrate stability based on a joint analysis of the near-bottom temperatures measured by CTDs, a bathymetric database, and theoretical hydrate stability conditions. Maps like these can provide more detailed information about landward limits of gas hydrate stability than can analyses of average water column temperatures in global grids (Figure 25).

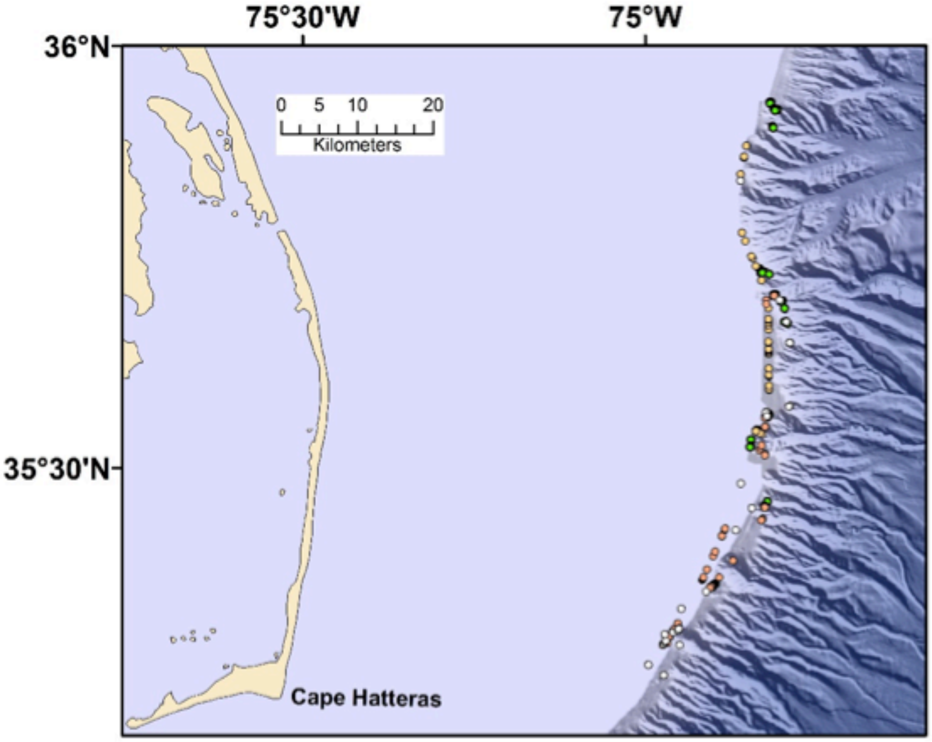

Figure 28. Example of potential seepage locations that enhance the original Skarke et al. [2014] seeps database (green circles) for the USAM. This shallow area near the shelf-break near Cape Hatteras was surveyed by the USGS aboard a *R/V Armstrong* science verification cruise in 2016 and identified new seeps shown here in white. In 2017, an *R/V Hugh R. Sharp* cruise identified potential seepage (not yet fully verified) at many other locations (orange) on the outer slope. Even if only a fraction of these locations can be shown to be robustly seeping, clearly methane emissions are far more widespread on this part of the margin than previously believed.

4 Journal publications, conference papers, and presentations

4.1 Journal publications

- Brothers, D.S., Ruppel, C., Kluesner, J.W., ten Brink, U.S., Chaytor, J.D., Hill, J.C., Andrews, B.D. and Flores, C., 2014, Seabed fluid expulsion along upper slope and outer shelf of the U.S. Atlantic continental margin. *Geophys. Res. Lett.*, doi: 10.1002/2013GL058048.

- Skarke, A., C. Ruppel, M. Kodis, D. Brothers, and E. Lobecker, 2014, Widespread methane leakage from the seafloor on the northern US Atlantic margin, *Nature Geoscience*, doi:10.1038/ngeo2232.

- L. Cueto-Felgueroso and R. Juanes. A phase-field model of two-phase Hele-Shaw flow. *J. Fluid Mech.*, 758, 522-552 (2014), doi:10.1017/jfm.2014.512.

- Weber, T., Mayer, L., Jerram, K., Beaudoin, J., Rzhanov, Y. and Lovalvo, D., 2014. Acoustic estimates of methane gas flux from the seabed in a 6000 km2 region in the Northern Gulf of Mexico. *Geochemistry, Geophysics, Geosystems.* 15(5): 1911-1925 (2014), doi:10.1002/2014GC005271.

- A. Alizadeh Pahlavan, L. Cueto-Felgueroso, G. H. McKinley and R. Juanes. Thin films in partial wetting: internal selection of contact-line dynamics. *Physical Review Letters*, 115, 034502 (2015), doi:10.1103/PhysRevLett.115.034502.

- Weinstein, A., L. Navarrete, C. Ruppel, T. C. Weber, M. Leonte, M. Y. Kellermann, E. C. Arrington, D. L. Valentine, M. I. Scranton, and J. D. Kessler. Determining the flux of methane into Hudson Canyon at the edge of methane clathrate hydrate stability, *Geochem. Geophys. Geosyst.*, 17, 3882–3892 (2016), doi:10.1002/2016GC006421.

- X. Fu, L. Cueto-Felgueroso, and R. Juanes. Thermodynamic coarsening arrested by viscous fingering in partially-miscible binary mixtures. *Physical Review E*, 94, 033111 (2016), doi:10.1103/PhysRevE.94.033111.

- Ruppel, C. D., and J. D. Kessler. The interaction of climate change and methane hydrates, *Rev. Geophys.*, 54 (2016), doi:10.1002/2016RG000534.

- X. Fu, L. Cueto-Felgueroso, and R. Juanes. Viscous fingering with partially miscible fluids. *Physical Review Fluids*, 2, 104001 (2017), doi:10.1103/PhysRevFluids.2.104001.

- X. Fu, L. Cueto-Felgueroso, and R. Juanes. Nonequilibrium thermodynamics of hydrate growth on a gas–liquid interface. *Physical Review Letters*, 120, 144501 (2018), doi:10.1103/PhysRevLett.12

4.2 Conference papers

- Waite, W.F., Weber, T., Fu, X., Juanes, R., Ruppel, C., Laboratory determination of rise rates for bubbles with and without hydrate shells, 9th International Conference on Gas Hydrates, Denver, CO, June 25-30, 2017.

4.3 Presentations

- Brothers, D., Ruppel, Kluesner, Chaytor, ten Brink, and Hill, 2013, Pervasive evidence for seabed fluid expulsion along upper slope of the US Atlantic continental margin, EOS Trans AGU, OS21A-1614, Fall Meeting, 2013.
- Kodis, M., Skarke, Ruppel, Weber, Lobecker, and Malik, 2013, US Atlantic margin methane plumes identified from water column backscatter data acquired by NOAA ship Okeanos Explorer, EOS Trans. AGU, OS21A-1612, Fall AGU Meeting (poster).
- Skarke, A., Ruppel, Kodis, Lobecker, and Malik, 2013, Geological significance of newly discovered methane seeps on the northern US Atlantic margin, EOS Trans. AGU, OS21A-1613, AGU Fall Meeting (poster).
- Scandella, Urban, Delwiche, Greinert, Hemond, Ruppel, and Juanes, 2013, Quantifying methane flux from lake sediments using multibeam sonar, EOS Trans AGU, B53B-0456, Fall Meeting, 2013.
- Ruppel, 2014, Gas seeps on the US Atlantic margin, NOAA Education & Outreach videotaped talk, March 2014 (invited).
- Ruppel, 2014, Exploration in the Atlantic Canyons, NOAA OER Conference and Review, Baltimore, MD, September 2014 (invited).
- Ruppel, Weber, Kessler, Pohlman, and Skarke, Methane hydrate dissociation and gas seepage on global upper continental slopes driven by intermediate ocean warming, EOS Trans. AGU, OS11C-01, AGU Fall Meeting.
- Ruppel, Skarke, Kodis, and D. Brothers, 2014, Hundreds of seeps on the northern US Atlantic margin: Evidence for warming-induced gas hydrate breakdown, US Geological Survey Santa Cruz, June 2014.
- Ruppel, Skarke, Kodis, D. Brothers, and Lobecker, 2014, Methane seepage at $\sim$600 newly-discovered sites between Cape Hatteras and Georges Bank, URI Graduate School of Oceanography weekly seminar series, October 2014.
- Benjamin P. Scandella, Liam Pillsbury, Thomas Weber, Carolyn D. Ruppel, Harry Hemond, Ruben Juanes. Quantitative spatiotemporal characterization of methane venting from lake sediments. EOS Trans. AGU B13D-0208, AGU Fall Meeting 2014.
- Xiaojing Fu, Luis Cueto-Felgueroso, William F. Waite, Carolyn D. Ruppel, Ruben Juanes. A Phase-Field Approach to Modeling Hydrate Formation on Methane Gas Bubbles in a Water Column. EOS Trans. AGU OS21B-1119A, AGU Fall Meeting 2014.
- Benjamin P. Scandella, Liam Pillsbury, Thomas Weber, Carolyn D. Ruppel, Harry Hemond, Ruben Juanes. Spatiotemporal signature of methane venting from lake sediments: from lab to field scale. EOS Trans. AGU B51F-0485, AGU Fall Meeting 2015.
- Xiaojing Fu, Luis Cueto-Felgueroso, Ruben Juanes. Viscous fingering with partially miscible fluids. EOS Trans. AGU H41D-1356, AGU Fall Meeting 2015.

- X. Fu, L. Cueto-Felgueroso, R. Juanes, Crustal fingering: solidification of a moving interface. Presentation G1.00003, APS Division of Fluid Dynamics Meeting 2016.
- L. Cueto-Felgueroso, X. Fu, R. Juanes. Modeling multiphase, multicomponent flows at the pore scale: Wetting phenomena and non-equilibrium phase behavior. EOS Trans. AGU H44C-04, AGU Fall Meeting 2016.
- X. Fu, J. Jimenez-Martinez, M. Porter, L. Cueto-Felgueroso, R. Juanes, Experiments and phase-field modeling of hydrate growth at the interface of migrating gas fingers. EOS Trans. AGU OS54A-01, AGU Fall Meeting 2016.
- Weber, T., Acoustic observations and characterization of oceanic methane gas bubbles rising from the seabed, 172nd Meeting of the Acoustical Society of America, 28 November – 2 December, 2016, Honolulu, Hawaii. This lecture was the *Medwin Prize in Acoustical Oceanography given by ASA* (http://acousticalsociety.org/funding_resources/prizes).
- William F. Waite. Methane gas hydrates: A tale of bubbles great and small. Invited talk for the U. New Hampshire Center for Coastal and Ocean Mapping Seminar series. April 7, 2017.
- X. Fu, J. Jimenez-Martinez, M. Porter, L. Cueto-Felgueroso, R. Juanes, Experiments and phase-field modeling of hydrate growth at the interface of migrating gas fingers, 9th International Conference on Gas Hydrates, Denver, CO, June 25-30, 2017.
- J. Jimenez-Martinez, M. Porter, X. Fu, L. Cueto-Felgueroso, H. S. Viswanathan, J. W. Carey, R. Juanes, Physics of hydrate-encrusted bubbles during depressurization: Insights from 2D experiments and phase-field modeling, 9th International Conference on Gas Hydrates, Denver, CO, June 25-30, 2017.
- Ruben Juanes, Xiaojing Fu, Luis Cueto-Felgueroso, Pore-scale modeling of phase change in porous media, 70th Annual Meeting of the APS Division of Fluid Dynamics, Denver, Colorado, November 19–21, 2017.
- Xiaojing Fu, Joaquin Jimenez-Martinez, Luis Cueto-Felgueroso, Mark Porter, Ruben Juanes, Crustal fingering: solidification on a viscously unstable interface, 70th Annual Meeting of the APS Division of Fluid Dynamics, Denver, Colorado, November 19–21, 2017.

References

H. K. Abay and T. M. Svartaas. On the kinetics of methane hydrate formation: a time-dependent kinetic rate model. In *Proceedings of the 7th International Conference on Gas Hydrates*, 2011.

Y. Abe, X. Ma, T. Yanai, and K. Yamane. Development of formation and growth models of CO2 hydrate film. *AIChE J.*, 62(11):4078–4089, 2016.

D. M. Anderson, G. B. McFadden, and A. A. Wheeler. Diffuse-interface methods in fluid mechanics. *Annu. Rev. Fluid Mech.*, 30(1):139–165, January 1998.

Karin Andreassen, Alun Hubbard, Monica C.M. Winsborrow, Henry Patton, Sunil Vadakkepuliyambatta, Andreia Plaza-Faverola, Eythor Gudlaugsson, Pavel Serov, A. Deryabin, Rune Mattingsdal, Jürgen Mienert, and Stefan Bünz. Massive blow-out craters formed by hydrate-controlled methane expulsion from the Arctic seafloor. *Science*, 356:948–953, 2017.

Lee E. Baker, Alan C. Pierce, and Kraemer D. Luks. Gibbs Energy Analysis of Phase Equilibria. *Soc. Petrol. Eng. J.*, 22(5):731–742, 1982.

A. L. Ballard and E. D. Sloan. The next generation of hydrate prediction IV: A comparison of available hydrate prediction programs. *Fluid Phase Equilib.*, 216(2):257–270, 2004.

Ballard, A. L. and E. D. Sloan. The next generation of hydrate prediction: Part III. Gibbs energy minimization formalism. *Fluid Phase Equilib.*, 218(1):15–31, 2004.

N. L. B. Bangs, M. J. Hornbach, and C. Berndt. The mechanics of intermittent methane venting at South Hydrate Ridge inferred from 4D seismic surveying. *Earth Planet. Sci. Lett.*, 310(1): 105–112, 2011.

C. Berndt, T. Feseker, T. Treude, S. Krastel, V. Liebetrau, H. Niemann, V. J. Bertics, I. Dumke, K. Dunnbier, B. Ferre, C. Graves, F. Gross, K. Hissmann, V. Huhnerbach, S. Krause, K. Lieser, J. Schauer, and L. Steinle. Temporal constraints on hydrate-controlled methane seepage off Svalbard. *Science*, 343:284–287, 2014.

A. J. Bray. Theory of phase ordering kinetics. *Adv. Phys.*, 43:357–459, 1994.

W. S. Burdic. *Underwater Acoustic System Analysis*. Prentice Hall, 1991.

J. W. Cahn and J. E. Hilliard. Free energy of a nonuniform system. I. Interfacial free energy. *J. Chem. Phys.*, 28(2):258, 1958.

M. Chaouachi, A. Falenty, K. Sell, F. Enzmann, M. Kersten, D. Harberthür, and W. Kuhs. Microstructural evolution of gas hydrates in sedimentary matrices observed with synchrotron X-ray computed tomographic microscopy. *Geochem. Geophys. Geosys.*, 16:1711–1722, 2015.

L. Chen, J. S. Levine, M.W. Gilmer, E. Dendy Sloan, C. A. Koh, and A. K. Sum. Methane hydrate formation and dissociation on suspended gas bubbles in water. *J. Chem. Eng. Data*, 59(4): 1045–1051, 2014.

L. Chen, J. S. Levine, M.W. Gilmer, E. Dendy Sloan, C. A. Koh, and A. K. Sum. Correction to "Methane hydrate formation and dissociation on suspended gas bubbles in water". *J. Chem. Eng. Data*, 61(7):2647–2647, 2016.

C. Clay and H. Medwin. *Acoustical Oceanography: Principles and Applications*. John Wiley & Sons, 1977.

M. Ben Clennell, Martin Hovland, James S. Booth, Pierre Henry, and William J. Winters. Formation of natural gas hydrates in marine sediments: 1. Conceptual model of gas hydrate growth conditioned by host sediment properties. *J. Geophys. Res.*, 104(B10):22985, 1999.

J. Clerk-Maxwell. On the dynamical evidence of the molecular constitution of bodies. *Nature*, 11: 357–359, 1875.

R. Clift, J.R. Grace, and M.E. Weber. *Bubbles, Drops, and Particles*. Academic Press, 1978.

D. A. Cogswell and W. C. Carter. Thermodynamic phase-field model for microstructure with multiple components and phases: The possibility of metastable phases. *Phys. Rev. E*, 83(6): 1–13, 2011.

L. Cueto-Felgueroso and R. Juanes. Macroscopic phase-field model of partial wetting: bubbles in a capillary tube. *Phys. Rev. Lett.*, 108(14):144502, April 2012.

L. Cueto-Felgueroso and J. Peraire. A time-adaptive finite volume method for the Cahn-Hilliard and Kuramoto-Sivashinsky equations. *J. Comput. Phys.*, 227(24):9985–10017, December 2008.

D. A. Demer, L. Berger, M. Bernasconi, E. Bethke, K. Boswell, D. Chu, et al. Calibration of acoustic instruments. *ICES Cooperative Research Report*, 133, 2015.

L. Dimitrov and V. Dontcheva. Seabed pockmarks in the southern Bulgarian Black Sea zone. *Bull. Geol. Soc. Denmark*, 41:24–33, 1994.

C. L. Van Dover et al. Blake Ridge methane seeps: geological and biological contexts. *Deep Sea Res.*, 50:281–300, 2003.

R. Embley. Water column and cold seep exploration of the Cascadia Margin. *Oceanography (Supplement)*, 30:94, 2017.

Expedition EX1402L3 Scientists. Okeanos Explorer EX1402L3: Gulf of Mexico 2014 Expedition Dive 01: Site GB648. 2014.

R. Folch and M. Plapp. Quantitative phase-field modeling of two-phase growth. *Phys. Rev. E*, 72 (1):011602, 2005.

R. Folch, J. Casademunt, A. Hernández-Machado, and L. Ramirez-Piscina. Phase-field models for Hele-Shaw flows with arbitrary viscosity contrast. I. theoretical approach. *Phys. Rev. E*, 60: 1724–1733, 1999a.

R. Folch, J. Casademunt, A. Hernández-Machado, and L. Ramirez-Piscina. Phase-field models for Hele-Shaw flows with arbitrary viscosity contrast. II. numerical study. *Phys. Rev. E*, 60: 1734–1740, 1999b.

Erik M. Freer, M.S. Selim, and E.D. Sloan. Methane hydrate film growth kinetics. *Fluid Phase Equilib.*, 185:65–75, 2001.

Fu, X., L. Cueto-Felgueroso, and R. Juanes. Thermodynamic coarsening arrested by viscous fingering in partial-miscible binary mixtures. *Phys. Rev. E*, 94(3):033111, 2016.

Fu, X., L. Cueto-Felgueroso, and R. Juanes. Viscous fingering with partially miscible fluids. *Phys. Rev. Fluids*, 2:104001, 2017.

Fu, X., L. Cueto-Felgueroso, and R. Juanes. Nonequilibrium thermodynamics of hydrate growth on a gas-liquid interface. *Phys. Rev. Lett.*, 120:144501, 2018.

H. Gomez and K. G. van der Zee. *Computational Phase-Field Modeling*. John Wiley & Sons, Ltd., 2015.

H. Gomez, T. J.R. Hughes, X. Nogueira, and V. M. Calo. Isogeometric analysis of the isothermal Navier-Stokes-Korteweg equations. *Comput. Meth. Appl. Mech. Eng.*, 199(25-28):1828–1840, May 2010.

R. R. Goodman and R. Stern. Reflection and transmission of sound by elastic spherical shells. *J. Acous. Soc. Amer.*, 34(3):338–344, 1962.

C. A. Graves, L. Steinle, G. Rehder, H. Niemann, D. P. Connelly, D. Lowry, R. E. Fisher, A. W. Stott, H. Sahling, and R. H. James. Fluxes and fate of dissolved methane released at the seafloor at the landward limit of the gas hydrate stability zone offshore western Svalbard. *J. Geophys. Res. Oceans*, 120(9):6185–6201, 2015.

J. Greinert, Y. Artemov, V. Egorov, M. De Batist, and D. McGinnis. 1300-m-high rising bubbles from mud volcanos at 2080 m in the Black Sea: Hydroacoustic characteristics and temporal variability. *Earth Planet. Sci. Lett.*, 244, 2006.

J. Greinert, K. B. Lewis, J. Bialas, I. A. Pecher, A. Rowden, D. A. Bowden, M. De Batist, and P. Linke. Methane seepage along the Hikurangi Margin, New Zealand: Overview of studies in 2006 and 2007 and new evidence from visual, bathymetric and hydroacoustic investigations. *Mar. Geol.*, 272:6–25, 2010a.

J. Greinert, D. F. McGinnis, L. Naudts, P. Linke, and M. De Batist. Atmospheric methane flux from bubbling seeps: Spatially extrapolated quantification from a Black Sea shelf area. *J. Geophys. Res.*, 115(C1):C01002, January 2010b.

J. Gros, C. M. Reddy, R. K. Nelson, S. A. Socolofsky, and J. S. Arey. Simulating gas?liquid?water partitioning and fluid properties of petroleum under pressure: implications for deep-sea blowouts. *Environ. Sci. Technol.*, 50(14):7397–7408, 2016.

J. Gros, S. A. Socolofsky, A. L. Dissanayake, I. Jun, L. Zhao, M. C. Boufadel, C. M. Reddy, and J. S. Arey. Petroleum dynamics in the sea and influence of subsea dispersant injection during Deepwater Horizon. *Proc. Natl. Acad. Sci. U.S.A.*, page doi:10.1073/pnas.1612518114, 2017.

L. P. Hauge, J. Gauteplass, M. D. Høyland, G. Ersland, A. Kovscek, and M. A. Fernø. Pore-level hydrate formation mechanisms using realistic rock structures in high-pressure silicon micromodels. *Int. J. Greenh. Gas Control*, 53:178–186, 2016.

K. U. Heeschen, A. M. Trehu, R. W. Collier, E. Suess, and G. Rehder. Distribution and height of methane bubble plumes on the Cascadia Margin characterized by acoustic imaging. *Geophys. Res. Lett.*, 30(12):1643, doi:10.1029/2003GL016974, 2003.

A. Hernández-Machado, M. Lacasta, E. Mayoral, and E. Corvera-Poiré. Phase-field model of Hele-Shaw flows in the high-viscosity contrast regime. *Phys. Rev. E*, 68:046310, 2003.

W. S. Holbrook, H. Hoskins, W. T. Wood, R. A. Stephen, and D. Lizarralde. Methane hydrate and free gas on the Blake Ridge from vertical seismic profiling. *Science*, 273:1840–1842, 1996.

J. Hornafius, D. Quigley, and B. Luyendyk. The world's most spectactular marine hydrocarbon seeps (Coal Oil Point, Santa Barbara Channel, California): quantification of emission. *J. Geophys. Res.*, 104:20703–20711, 1999.

Z. Huo, K. Hester, E. D. Sloan, and K. T. Miller. Methane hydrate nonstoichiometry and phase diagram. *AIChE J.*, 49(5):1300–1306, 2003.

IPCC. *Climate Change 2001: The Scientific Basis*. Cambridge University Press, Cambridge, UK, 2001.

David Jacqmin. Calculation of two-phase Navier–Stokes flows using phase-field modeling. *J. Comput. Phys.*, 155(1):96–127, 1999.

M. Jamialahmadi, C. Branch, and J. Müller-Steinhagen. Terminal bubble rise velocity in liquids. *Trans. AIChE*, 72:119–122, 1994.

J. M. Jech, J. K. Horne, D. Chu, D. A. Demer, D. T. Francis, N. Gorska, et al. Comparisons among ten models of acoustic backscattering used in aquatic ecosystem research. *J. Acoust. Soc. Am.*, 138(6):3742–3764, 2015.

K. Jerram, T. Weber, and J. Beaudoin. Split?beam echo sounder observations of natural methane seep variability in the Northern Gulf of Mexico. *Geochem. Geophys. Geosys.*, 16(3):736–750, 2015.

H. P. Johnson, U. K. Miller, M. S. Salmi, and E. A. Solomon. Analysis of bubble plume distributions to evaluate methane hydrate decomposition on the continental slope. *Geochem. Geophys. Geosys.*, 16:3825–3839, 2015.

P. K. Kannberg, A. M. Tréhu, S. D. Pierce, C. K. Paull, and D. W. Caress. Temporal variation of methane flares in the ocean above Hydrate Ridge, Oregon. *Earth Planet. Sci. Lett.*, 368:33–42, 2013.

I. Leifer and I. MacDonald. Dynamics of the gas flux from shallow gas hydrate deposits: interaction between oily hydrate bubbles and the oceanic environment. *Earth Planet. Sci. Lett.*, 210 (3–4):411–424, 2003.

S. L. Li, C. Y. Sun, B. Liu, X. J. Feng, F. G. Li, L. T. Chen, and G. J. Chen. Initial thickness measurements and insights into crystal growth of methane hydrate film. *AIChE J.*, 59(6):2145–2154, 2013.

J. Liu, C. M. Landis, H. Gomez, and T. J. R. Hughes. Liquid–vapor phase transition: thermomechanical theory, entropy stable numerical formulation, and boiling simulations. *Comput. Methods Appl. Mech. Engrg.*, 297:476–553, 2015.

Xiaoli Liu and Peter B. Flemings. Passing gas through the hydrate stability zone at southern Hydrate Ridge, offshore Oregon. *Earth Planet. Sci. Lett.*, 241(1-2):211–226, 2006.

T. D. Lorenson, I. Leifer, F. L. Wong, R. J. Rosenbauer, P. L. Campbell, A. Lam, F. D. Hostettler, J. Greinert, D. P. Finlayson, E. S. Bradley, and B. P. Luyendyk. Biomarker chemistry and flux quantification methods for natural petroleum seeps and produced oils, offshore southern California. U.S. Geological Survey Scientific Investigations Report 2011?5210, 45 p., 4 data files and OCS Study BOEM 2011?016, available at http://pubs.usgs.gov/sir/2011/5210/, 2016.

J. Lowengrub and L. Truskinovsky. Quasi-incompressible Cahn-Hilliard fluids and topological transitions. *Proc. R. Soc. Lond. A*, 454:2617–2654, 1998.

B. B. Maini and P. R. Bishnoi. Experimental investigation of hydrate formation behaviour of a natural gas bubble in a simulated deep sea environment. *Chem. Eng. Sci.*, 36:183–189, 1981.

S. Mau, D. L. Valentine, J. F. Clark, J. Reed, R. Camilli, and L. Washburn. Dissolved methane distributions and air-sea flux in the plume of a massive seep field, Coal Oil Point, California. *Geophys. Res. Lett.*, 34(22):L22603, 2007.

I. R. McDonald, I. L. R. Sassen, P. Stine, R. Mitchell, and N. J. Guinasso. Transfer of hydrocarbons from natural seeps to the water column and atmosphere. *Geofluids*, 2:95–107, 2002.

D. F. McGinnis, J. Greinert, Y. Artemov, S. E. Beaubien, and a. Wüest. Fate of rising methane bubbles in stratified waters: How much methane reaches the atmosphere? *J. Geophys. Res.*, 111 (C9):C09007, 2006.

R. Merewether, M. S. Olsson, and P. Lonsdale. Acoustically detected hydrocarbon plumes rising from 2-km depths in the Guayamas Basin, Gulf of California. *J. Geophys. Res.*, 90:3075–3085, 1985.

Merle, S. and Embley, R. NA72-Seeps and Ecosystems of the Cascadia Margin, June 1-20, 2016 Victoria BC, Canada to San Francisco CA, USA (cruise report of the E/V Nautilus). 2016.

M. Michelsen and J. Mollerup. *Thermodynamic Models: Fundamentals & Computational Aspects*. Tie-Line Publications, Copenhagen, 2007.

N. Moelans. A quantitative and thermodynamically consistent phase-field interpolation function for multi-phase systems. *Acta Mater.*, 59(3):1077–1086, 2011.

J. M. Mogollón, A. W. Dale, I. L'Heureux, and P. Regnier. Impact of seasonal temperature and pressure changes on methane gas production, dissolution, and transport in unfractured sediments. *J. Geophys. Res.*, 116:doi:10.1029/2010JG001592, 2011.

B. Nestler, A. A. Wheeler, L. Ratke, and C. Stöcker. Phase-field model for solidification of a monotectic alloy with convection. *Physica D*, 141:133–154, 2000.

K. Ohgaki, T. Sugahara, M. Suzuki, and H. Jindai. Phase behavior of xenon hydrate system. *Fluid Phase Equilib.*, 175(1-2):1–6, 2000.

B. Peters, N. E. R. Zimmermann, G. T. Beckham, J. W. Tester, and B. L. Trout. Path sampling calculation of methane diffusivity in natural gas hydrates from a water-vacancy assisted mechanism. *J. Am. Chem. Soc.*, 130(51):17342–17350, 2008.

L. Pillsbury. Characterizing and quantifying marine methane gas seeps using acoustic observations and bubble dissolution models. Master's thesis, University of New Hampshire, 2015.

W. S. Reeburgh. Oceanic methane biogeochemistry. *Chem. Rev.*, 107:486–513, 2007.

G. Rehder, P. W. Brewer, E. T. Peltzer, and G. Friederich. Enhanced lifetime of methane bubble streams within the deep ocean. *Geophys. Res. Lett.*, 29(15):21–1–21–4, August 2002.

G. Rehder, I. Leifer, P. G. Brewer, G. Friederich, and E. T. Peltzer. Controls on methane bubble dissolution inside and outside the hydrate stability field from open ocean field experiments and numerical modeling. *Mar. Chem.*, 114(1-2):19–30, 2009.

M. Römer, H. Sahling, T. Pape, G. Bohrmann, and V. Spieβ. Quantification of gas bubble emissions from submarine hydrocarbon seeps at the makran continental margin (offshore pakistan). *J. Geophys. Res. Oceans*, 117(C10), 2012.

J. S. Rowlinson. Translation of J. D. van der Waals' "The thermodynamik theory of capillarity under the hypothesis of a continuous variation of density". *J. Stat. Phys.*, 20(2):197–200, 1979.

C. Ruppel. Permafrost-associated gas hydrate: Is it really approximately 1% of the global system? *J. Chem. Eng. Data*, 6:429–436, 2015.

C. Ruppel and J. D. Kessler. The interaction of climate change and methane hydrates. *Rev. Geophys.*, 55:126–168, 2017.

C. Ruppel, J. Kluesner, J. Pohlman, D. Brothers, F. Colwell, S. Krause, and T. Treude. Methane hydrate dynamics on the Northern US Atlantic margin. *Fire in the Ice*, pages 10–13, 2015.

C. Ruppel, A. Demopoulos, and N. Prouty. Exploring US Mid-Atlantic Margin Methane Seeps: IMMeRSS, May 2017. *Oceanography (Supplement)*, 31(1):97, 2018.

K. Saito, A. K. Sum, and R. Ohmura. Correlation of hydrate-film growth rate at the guest/liquid-water interface to mass transfer resistance. *Ind. Eng. Chem. Res.*, 49(15):7102–7103, 2010.

E. J. Sauter, S. I. Muyakshin, J.-L. Charlou, M. Schlüter, A. Boetius, K. Jerosch, E. Damm, J.-P. Foucher, and M. Klages. Methane discharge from a deep-sea submarine mud volcano into the upper water column by gas hydrate-coated methane bubbles. *Earth Planet. Sci. Lett.*, 243(3-4): 354–365, March 2006.

O. Sifner and J. Klomfar. Thermodynamic properties of xenon from the triple point to 800 K with pressures up to 350 MPa. *J. Phys. Chem. Ref. Data*, 23:63–152, 1994.

A. Skarke, C. Ruppel, M. Kodis, D. Brothers, and E. Lobecker. Widespread methane leakage from the sea floor on the northern US Atlantic margin. *Nat. Geosci.*, 7:657–661, 2014.

E. D. Sloan. Fundamental principles and applications of natural gas hydrates. *Nature*, 426(6964): 353–63, 2003.

E. D. Sloan and C. A. Koh. *Clathrate Hydrates of Natural Gases*. CRC Press, Boca Raton, FL, USA, 3rd edition, 2008.

E. D. Sloan, C. A. Koh, and A. K. Sum. Gas hydrate stability and sampling: the future as related to the phase diagram. *Energies*, 3(12):1991–2000, 2010.

S. A. Socolofsky, A. L. Dissanayake, I. Jun, J. Gros, J. S. Arey, and C. M. Reddy. Texas A&M Oilspill Calculator (TAMOC): Modeling Suite for Subsea Spills. In *38th AMOP Technical Seminar on Environmental Contamination and Response*, pages 2–4, Vancouver, BC, Canada, 2015.

T. K. Stanton. Sound scattering by spherical and elongated shelled bodies. *J. Acoust. Soc. Am.*, 88 (3):1619–1633, 1990.

E. Suess, M. E. Torres, G. Bohrmann, R. W. Collier, J. Greinert, P. Linke, G. Rehder, A. Trehu, K. Wallmann, G. Winckler, and E. Zuleger. Gas hydrate destabilization: enhanced dewatering, benthic material turnover and large methane plumes at the Cascadia convergent margin. *Earth Planet. Sci. Lett.*, 170(1-2):1–15, 1999.

Y. Sun and C. Beckermann. Phase-field modeling of bubble growth and flow in a Hele-Shaw cell. *Int. J. Heat Mass Transfer*, 53(15-16):2969–2978, July 2010.

A. Svandal, T. Kuznetsova, and B. Kvamme. Thermodynamic properties and phase transtions in the $H_2O/CO_2/CH_4$ system. *Phys. Chem. Chem. Phys.*, 8(14):1707–13, 2006.

A. Svandal, T. Buanes, and T. Kuznetsova. Phase field approaches to the kinetic modeling of hydrate phase transitions. In *Natural gas hydrates–Energy resource potential and associated geologic hazards: AAPG Memoir*, volume 89, pages 758–769, 2009.

Ryo Tanaka, Riki Sakemoto, and Ryo Ohmura. Crystal growth of clathrate hydrates formed at the interface of liquid water and gaseous methane, ethane, or propane: Variations in crystal morphology. *Cryst. Growth Des.*, 9(5):2529–2536, 2009.

Tap Plastics. Acrylic rod and tube technical data. 2015.

C. J. Taylor, K. T. Miller, C. A. Koh, and E. D. Sloan. Macroscopic investigation of hydrate film growth at the hydrocarbon/water interface. *Chem. Eng. Sci.*, 62(23):6524–6533, December 2007.

G. Tegze, T. Pusztai, and L. Gránásy. Phase field simulation of liquid phase separation with fluid flow. *Mater. Sci. Eng., A*, 413-414:418–422, 2005.

B. Tohidi, R. Anderson, M. B. Clennell, R. W. Burgass, and A. B. Biderkab. Visual observation of gas-hydrate formation and dissociation in synthetic porous media by means of glass micromodels. *Geology*, 29(9):867, 2001.

D. R. Topham. The formation of gas hydrates on bubbles of hydrocarbon gases rising in seawater. *Chem. Eng. Sci.*, 39(5):821–828, 1984.

D. L. Valentine, D. C. Blanton, W. S. Reeburgh, and M. Kastner. Water column methane oxidation adjacent to an area of active hydrate dissociation, Eel River Basin. *Geochim. Cosmochim. Acta*, 65:2633–2640, 2001.

J. D. van der Waals. *Z. Phys. Chem.*, 13:657, 1894.

W. F. Waite, M. B. Helgerud, A. Nur, J. C. Pinkston, L. A. Stern, S. H. Kirby, and W. B. Durham. Laboratory measurements of compressional and shear wave speeds through methane hydrate. *Annals of the New York Academy of Sciences*, 912:1003–1010, 2000.

W.F. Waite, T. Weber, X. Fu, R. Juanes, and C. Ruppel. Laboratory observations of the evolution and rise rate of bubbles with and without hydrate shells. In *Proceedings of the 9th International Conference on Gas Hydrates*, 2017.

B. Wang and Socolofsky. A deep-sea, high-speed, stereoscopic imaging system for in situ measurement of natural seep bubble and droplet characteristics. *Deep-Sea Res.*, 104:134–148, 2015.

B. Wang, S. Socolofsky, J. Breier, and J. Seewald. Observations of bubbles in natural seep flares at MC 118 and GC 600 using in situ quantitative imaging. *J. Geophys. Res. Oceans*, 121, 2016.

R. P. Warzinski, R. Lynn, I. Haljasmaa, I. Leifer, F. Shaffer, B. J. Anderson, and J. S. Levine. Dynamic morphology of gas hydrate on a methane bubble in water: Observations and new insights for hydrate film models. *Geophys. Res. Lett.*, 41, sep 2014.

R. C. Weast, M. J. Astle, W. H. Beyer, et al. *CRC Handbook of Chemistry and Physics*, volume 1990. CRC press, Boca Raton, FL, 1989.

T. Weber, L. Mayer, K. Jerram, J. Beaudoin, Y. Rzhanov, and D. Lovalvo. Acoustic estimates of gas flux from a 6000 km2 region in the Northern Gulf of Mexico. *Geochem. Geophys. Geosys.*, 15(5):1911–1925, 2014.

A. Weinstein, L. Navarrete, C. Ruppel, T. C. Weber, M. Leonte, M. Y. Kellermann, E. C. Arrington, D. L. Valentine, M. I. Scranton, and J. D. Kessler. Determining the flux of methane into hudson canyon at the edge of methane clathrate hydrate stability. *Geochem., Geophys., Geosyst.*, 17 (10), 2016.

M. Weiss. Analysis of some modified cell-averaging CFAR processors in multiple-target situations. *IEEE Transactions on Aerospace and Electronic Systems*, pages 102–114, 1982.

G. K. Westbrook, K. E. Thatcher, E. J. Rohling, A. M. Piotrowski, H. Pälike, A. H. Osborne, E. G. Nisbet, T. A. Minshull, M. Lanoisellé, R. H. James, V. Hühnerbach, D. Green, R. E. Fisher, A. J. Crocker, A. Chabert, C. Bolton, A. Beszczynska-Möller, C. Berndt, and A. Aquilina. Escape of methane gas from the seabed along the West Spitsbergen continental margin. *Geophys. Res. Lett.*, 36(15):L15608, August 2009.

G. Wilson. A new expression for the excess free energy of mixing. *J. Am. Chem. Soc.*, 86(2): 127–130, 1964.

P. A. Witherspoon and D. N. Saraf. Diffusion of Methane, Ethane, Propane, and n-Butane. *J. Phys. Chem.*, 69(11):3752–3755, 1965.

N. Wüstneck, R. Wüstneck, U. Pison, and H. Möhwald. On the dissolution of vapors and gases. *Langmuir*, 23:1815–1823, 2007.

Y. Zhang. Methane escape from gas hydrate systems in marine environment, and methane-driven oceanic eruptions. *Geophys. Res. Lett.*, 30(7):1398, doi:10.1029/2002GL016658, 2003.